Measurement report: Intensive biomass burning emissions and rapid nitrate formation drive severe haze formation in Sichuan basin, China: insights from aerosol mass spectrometry

Zhier Bao[1], Xinyi Zhang[1], Qing Li[1], Jiawei Zhou[1], Guangming Shi[2], Li Zhou[2], Fumo Yang[2], Shaodong Xie[3], Dan Zhang[4], Chongzhi Zhai[4], Zhenliang Li[4], Chao Peng[4], and Yang Chen[1]

[1] Chongqing Institute of Green and Intelligent Technology, Chinese Academy of Sciences, Chongqing, 400714, China

[2] Department of Environmental Science and Engineering, College of Architecture and Environment, Sichuan University, Chengdu 610065, China

[3] SKL-ESPC and BIC-ESAT, College of Environmental Sciences and Engineering, Peking University, Beijing 100871, China

[4] Academy of Environmental Science, Chongqing, 401147, China

Correspondence: Yang Chen (chenyang@cigit.ac.cn)

Abstract

Haze pollution is a severe environmental problem, caused by elevation of fine particles (aerodynamic diameter < 2.5 μm, $PM_{2.5}$), which is related to secondary aerosol formation, unfavourable synoptic conditions, regional transport, etc. The regional haze formation in basin areas, along with intensive emission of precursors, high relative humidity and poor dispersion conditions, is still limitedly understood.In this study, a field campaign was conducted to investigate the factors resulting in haze formation in Sichuan Basin (SCB) during winter in 2021. The fine aerosol chemical composition was characterised by using a time-of-flight aerosol chemical speciation monitor (ToF-ACSM), which also provided detailed information on the sources for organic aerosols (OA). The average concentration of non-refractory fine particles (NR-$PM_{2.5}$) was 98.5 ± 38.7 μg/m^3, and organics aerosols, nitrate, sulphate, ammonium, and chloride took up 40.3, 28.8, 10.6, 15.3 and 5.1 % of $PM_{2.5}$. Three factors, including a hydrocarbon-like OA (HOA), a biomass burning OA (BBOA), and an oxygenated OA (OOA), were identified by applying the positive matrix factorisation (PMF)

28 analysis, and they constituted 24.2, 24.2 and 51.6 % of OA on average, respectively. Nitrate

29 formation was promoted by gas-phase and aqueous-phase oxidation, while sulphate was mainly

30 formed through aqueous-phase process. OOA showed strong dependence on Ox, demonstrating the

31 contribution of photooxidation to OOA formation. OOA concentration increased as aerosol liquid

32 water content (ALWC) increased within 200 μg/m^3 and kept relatively constant when ALWC > 200

33 μg/m^3, suggesting the insignificant effect of aqueous-phase reactions on OOA formation. Among

34 the three haze episodes identified during the whole campaign, the driving factors were different: the

35 first haze episode (H1) was driven by nitrate formation through photochemical and aqueous-phase

36 reactions, and the second haze episode (H2) was mainly driven by the intense emission of primary

37 organic aerosols from biomass burning and vehicle exhaust, while the third haze episode (H3) was

38 mainly driven by reactions involving nitrate formation and biomass burning emission. HOA and

39 BBOA were scavenged, while OOA, nitrate, and sulphate formation were enhanced by aqueous-

40 phase reactions during fog periods, which resulted in the increase of O:C from pre-fog to post-fog

41 periods. This study revealed the factors driving severe haze formation in SCB, and implied the

42 benefit of controlling nitrate as well as intense biomass burning and vehicle exhaust emission to the

43 mitigation of heavy aerosol pollution in this region.

44

45

46

1. Introduction

Although a series of emission reduction strategies had been implemented to mitigate severe haze pollution over a decade in China, the fine particle (particulate matter with aerodynamic diameter less than 2.5 μm, $PM_{2.5}$) pollution events still occurred, especially during autumn and winter (Ding et al., 2019; Zhao et al., 2020; Yan et al., 2020). Haze formation was affected by the intense emission of primary particles, rapid formation of secondary aerosols, stagnant meteorological conditions, and topography. The interplay among these factors usually makes haze formation complex (Bao et al., 2019; Guo et al., 2014; Zheng et al., 2015), which resulted in difficulties in making air pollution mitigation strategies.

Many studies showed that the rapid increase of secondary aerosols (including secondary inorganic/organic aerosols, i.e., SIA and SOA) played an important role in haze formation (Huang et al., 2014; Wu et al., 2022). Nitrate, sulphate, and ammonium, mainly formed through photochemical oxidation and aqueous-phase reactions in the atmosphere, were the major component of SIA. Previous studies demonstrated that the substantial formation of nitrate and sulphate exacerbated severe haze development (Wang et al., 2020; Liu et al., 2020). For example, Zheng et al. (2016) investigated the factors driving haze formation in Beijing in 2013, and the results showed that the enhanced production of sulphate and nitrate led to their increased contribution to $PM_{2.5}$ as the pollution level increased, while the contribution of organic matter (OM) decreased. The emission of SO_2 had been reduced dramatically over the past ten years in China; however, NOx did not show a significant reduction (Zhou et al., 2021; Liu et al., 2019). Thus, the haze formation was found to be mainly driven by the reactions generating nitrate in recent year (Fu et al., 2020; Li et al., 2018; Zhai et al., 2021).

Compared to SIA, the formation process of SOA was more complicated (Chen et al., 2017). For instance, SOA could be formed through the gas-phase photooxidation of volatile organic compounds (VOCs), which was affected by temperature, relative humidity (RH), and total organic aerosol mass loadings (Clark et al., 2016; Hinks et al., 2018; Donahue et al., 2006). SOA could also be formed through the oxidation of water-soluble VOCs or organic products of gas-phase photochemistry, which was observed in the field and laboratory studies (Liu et al., 2018; Chen et al., 2015). Besides, the aging of primary organic aerosols (POA) by oxidants in the atmosphere also

3

76   contributed to SOA (Wang et al., 2021; Gilardoni et al., 2016). For instance, the organic aerosols

77   emitted from biomass burning were oxidised through the photochemical oxidation process driven

78   by OH radicals which might take place in both gas and aqueous phases (Paglione et al., 2020). The

79   variations of regional and seasonal emissions might also affect the formation of SOA (Dai et al.,

80   2019; Sun et al., 2016). Thus, it is of vital importance to consider various factors when investigating

81   SOA formation.

82   Similar to the city clusters such as Beijing, Shanghai and Guangzhou in North China Plain

83   (NCP), Yangtze River Delta (YRD) and Pearl River Delta (PRD), the Chengdu-Chongqing city

84   cluster, located in the Sichuan Basin (SCB) in Southwest China, is also suffering severe haze

85   pollution (Tao et al., 2017; Tan et al., 2019). Many efforts had been made to investigate the temporal

86   variation, chemical composition and formation mechanism of $PM_{2.5}$ during the evolution of haze

87   episodes in NCP, YRD and PRD (Peng et al., 2021; Sun et al., 2016; Zhang et al., 2015; Yan et al.,

88   2020), whereas, only a few studies focused on the factors resulting in haze formation in SCB (Zhang

89   et al., 2019; Song et al., 2019). These studies mainly focused on the formation of inorganic species

90   in $PM_{2.5}$, and the results showed that the rapid formation of SIA under high RH conditions promoted

91   the increase of $PM_{2.5}$. However, further studies on the characteristics of OA, including the temporal

92   evolution, sources and formation pathways, are still lacking.

93   The area of SCB is ~260,000 km^2, and its population is ~110 million, making it an important

94   developing region in Southwest China. The basin is a subtropical expanse of low hills and plains

95   and is completely encircled by high mountains and plateaus, which is unfavourable for either

96   horizontal transport or vertical diffusion. The atmosphere in SCB was characterised by persistently

97   high relative humidity and low wind speed all year round. The haze evolution in SCB might be

98   different from those in other regions due to its unique topography, meteorological conditions and

99   emission sources, which remained unclear. Therefore, comprehensive studies are needed to reveal

100 the key factors contributing to haze formation in the basin (Wang et al., 2018).

101 The Time-of-Flight Aerosol Chemical Speciation Monitor (ToF-ACSM) is a robust and highly

102 sensitive instrument that provides real-time characterisation and composition of non-refractory

103 $PM_1/PM_{2.5}$ (NR-$PM_1/PM_{2.5}$) depending on the type of the aerodynamic lens used (Liu et al., 2007;

104 Xu et al., 2017). Compared to the Aerodyne aerosol spectrometer (AMS), the ToF-ACSM is more

105 compact and cheaper. However, the ToF-ACSM does not figure particle sizing. Compared to the

106 quadrupole-ACSM (Q-ACSM), the ToF-ACSM has better mass resolution and detection limits

107 (Fröhlich et al., 2013). Although the ToF-ACSM had not been widely deployed in field observations

108 as AMS/Q-ACSM did in a number of different sites over China, it had successfully characterised

109 the variation of $PM_1/PM_{2.5}$ and the sources of organic aerosols in the cities within NCP, YRD and

110 PRD (Ge et al., 2022; Sun et al., 2020; Guo et al., 2020). Despite this, few studies applied a Q/ToF-

111 ACSM or AMS in SCB. The responses of aerosol chemistry to meteorology and emissions therein

112 remained poorly understood. To the authors' best knowledge, this is the first time that the ToF-

113 ACSM has been deployed in the field observations within SCB.

114 The present study aims to uncover the factors driving severe haze formation during winter in

115 SBC. The characteristics of NR-$PM_{2.5}$, including mass concentration, chemical composition,

116 temporal and diurnal variation, were described in detail. The OA sources resolved by the positive

117 matrix factorisation (PMF) analysis and elemental composition were investigated to elucidate the

118 possible aging process of OA. The formation mechanism for SIA and SOA was also studied based

119 on the dependencies of nitrate, sulphate and OOA with odd oxygen ($Ox = O_3 + NO_2$) and aerosol

120 liquid water content. In addition, the evolution process of chemical composition and elemental

121 composition were summarised during different haze and fog episodes to investigate the main factors

122 exacerbating haze pollution. The data and results would fill the knowledge gap on the factors

123 affecting haze formation in SCB and provide a scientific basis for future air pollutant mitigation

124 strategies in this unique basin.

125 **2. Material and methods**

126 **2.1 Sampling site**

127 The field study was carried out from 18 December 2021 to 22 January 2022 at a site (30°55'59"

128 N, 104°12'25"E) in Deyang, and the site was near the northern border of Chengdu, the capital of

129 Sichuan province, China (as shown in Fig. 1). The site was located in a typical suburban region

130 surrounded by several food, aluminium alloy, and building materials factories. There was a main

131 road ~200 m south of the site. The north and west of the site were croplands and villages. Thus, the

132 site was affected by traffic emissions, biomass burning and industrial pollutants. The study at this

133 site would help to understand the characteristics of regional haze pollution and the influence of

134   regional transport between urban and suburban areas on haze formation

2.2 Instrumentation

136   During the campaign, the mass loadings of non-refractory organics, nitrate, sulphate,

137   ammonium and chloride in $PM_{2.5}$ were obtained online by a ToF-ACSM. The gaseous species,

138   including NO, NO_2, O_3, SO_2, CO and CO_2, were continuously measured by the Thermo gas

139   analysers (model 43i, 49i, 42i, 48i and 410i). The meteorological parameters, including temperature

140   (T), relative humidity (RH), solar radiation (SR), wind speed (WS) and wind direction (WD), were

141   obtained by an automatic weather station (Luff WS501-UMB).

142   For the NR-$PM_{2.5}$ measurement, the ambient air was pumped into the sampling line via a

143   vacuum pump, and the flow rate was maintained at 3 L/min with a flow meter. Before being sampled

144   by the ToF-ACSM, the ambient air would go through a $PM_{2.5}$ cyclone (URG-2000-30ED, USA) to

145   remove coarse particles, then was dried by a Nafion drier. The sampling line was assembled using

146   3/8' stainless steel tubes coated with the sponge to prevent water condensation.

147   The working principle of ToF-ACSM had been described in detail in previous studies (Ng et

148   al., 2011; Fröhlich et al., 2013). Briefly, a 100 μm critical orifice and an aerodynamic lens were

149   settled in the front inlet system to focus the ambient particles into a concentrated and narrow beam

150   with a flow rate of ~0.084 L/min. It should be mentioned that a $PM_{2.5}$ lens was used during the

151   whole campaign, which made the $PM_{2.5}$ measurement available (Xu et al., 2017).

152   The particle beam was transmitted through a vacuum chamber in which the gas-phase species

153   were separated from the particle beam. At the end of the vacuum chamber, the particles were

154   thermally vaporised at ~600 ℃ by impacting on a resistively heated porous tungsten surface. There

155   the non-refractory constituents in the particles flash vaporise and are subsequently ionised by a 70

156   eV electron impact. Finally, the ions were extracted by a set of ion optics and detected by the time-

157   of-flight mass spectrometer.

158   The ToF-ACSM was operated with a time resolution of 10 mins and scanned from m/z 10 to

159   219. The ionisation efficiency (IE) calibration was performed before and after the campaign

160   according to the proposal of a previous study (Fröhlich et al., 2013). Briefly, the size-selected (350

161   nm) NH_4NO_3 particles, which were generated by an aerosol generator, were simultaneously sampled

162   by the ToF-ACSM and a condensation particle counter (CPC 3775, TSI). Then, the IE can be

163   determined by comparing the response of ToF-ACSM to the mass of ammonium nitrate. The relative

164   ionisation efficiencies (RIEs) of sulphate and ammonium were also determined by sampling

165     $(NH_4)_2SO_4$ particles.

166   2.3 Data process

167   2.3.1 ToF-ACSM data analysis

168   The ToF-ACSM data analysis software (Tofware v2.5.13) written in Igor (Wavemetrics, Lake

169   Oswego, OR, USA) was used to analyse the mass concentration and chemical composition. The IE

170   value was 239 ions/pg, and the RIEs for sulphate and ammonium were 1.05 and 3.6, respectively.

171   For organics, nitrate and chloride, commonly used RIE values, i.e. 1.4, 1.1 and 1.3, were applied.

172   The algorithm proposed by Middlebrook et al. (2012) to determine the collection efficiency (CE) of

173   ToF-ACSM was applied to quantify the aerosol species, as the acidity, chemical composition, and

174   phase state changed the particle bounce effects at the vaporiser (Matthew et al., 2008).

175   The triangle plot of f44 (ratio of m/z 44 to total signal in the component mass spectrum) versus

176   f43 (ratio of m/z 43 to total signal in the component mass spectrum) and f44 versus f60 (ratio of m/z

177   60 to total signal in the component mass spectrum) were applied to characterise the evolution of OA

178   (Ng et al., 2010). The O/C and H/C were determined by the parameterization proposed by

179   Canagaratna et al. (2015).

180   2.3.2 PMF analysis

181   The mass spectrum data matrix of OA was analysed by the PMF Evaluation Tool (PET, v2.08D)

182   (Paatero and Tapper, 1994; Ulbrich et al., 2009) in order to resolve distinct OA factors that might

183   be representative of specific sources. The PMF-ACSM data processing was followed by the

184   procedures proposed previously (Ulbrich et al., 2009; Zhang et al., 2011). Due to the weak signal

185   intensities, the ions with m/z over 120 were not included in the analysis. Any ions with signal-to-

186   noise (S/N) < 0.2 were removed from the analysis, and the ions whose S/N was 0.2–2 were down-

187   weighted by increasing their errors calculations by a factor of 2 (Sun et al., 2011). Different PMF

188   solutions were resolved by varying the factor number from 2 to 7. The solutions were evaluated by

189   comparing the mass spectral profiles of the output secondary aerosol factors as a function of the

190   rotational parameter (fpeak). Finally, a three-factor solution with fpeak = 0 was selected as our best

191   solution. The comparison of the results for three to five-factor solutions was described in detail in

192   Fig. S4 and Table. S2.

193   **2.3.3 Identification of haze episodes**

194   The haze episodes were defined by the daily $PM_{2.5}$ mass concentration exceeding Grade II

195   National Ambient Air Quality Standard (AAQS) of 75 $\mu g/m^3$ for two successive days (Wang et al.,

196   2014). In the present study, we made some slight modifications to this definition following the

197   procedure of Zheng et al. (2016). Briefly, the periods during which the 24 h-moving average

198   concentration of $PM_{2.5}$ exceeds 75 $\mu g/m^3$ for two successive days are regarded as episode candidates.

199   If the hourly $PM_{2.5}$ concentration during the first hour of an episode candidate is 50-75 $\mu g/m^3$, then

200   the episode has a shape of 'slow start'; if it is 0-50 $\mu g/m^3$, then the episode has the shape of the 'rapid

201   start'. Similarly, the shape at the end of an episode candidate can also be identified. Haze episodes

202   having a 'slow start' typically arise from the gradual accumulation of pollutants emitted both locally

203   and regionally under unfavourable meteorological conditions, while haze episodes having a 'rapid

204   start' are most likely related to regional transport (Zheng et al., 2015). Haze episodes having a 'slow

205   end' usually resulted from the gradual scavenge of pollutants.

206   According to the definition mentioned above, three haze episodes (denoted as H1, H2 and H3,

207   respectively, in Fig. 2), all with the types of 'slow start' and 'slow end', were identified over the whole

208   campaign. In addition, a fog event occurred during each haze episode (denoted as F1, F2 and F3,

209   respectively). Lacking the information of visibility and aerosol size distribution up to several tens

210   of micrometres, we were not able to precisely diagnose the accumulation and dissipation stages of

211   a fog event. Instead, we selected the hours with RH near 100 % as the duration of a fog event, which

212   was the same as the condition described in previous studies (Izhar et al., 2020; Guo et al., 2015).

213   **2.4 Air parcels trajectories analysis**

214   2-day back trajectories arriving at the receptor site were calculated every hour over the whole

campaign using the National Oceanic and Atmospheric Administration (NOAA) HYSPLIT version
4 (Draxler and Hess, 1998). Input to the model is in the form of 1 ° latitude-longitude gridded
meteorological parameters from the Global Data Assimilation System meteorological dataset. We
chose an arrival height of 500 m which is above ground level (AGL) for target analysis in the
HYSPLIT model to diminish the effects of surface friction (Polissar et al., 2001); this height value
and greater are regarded as in the open height of the planetary boundary layer in winter and are more
useful for long-range transport. Finally, 839 backward trajectories in total were obtained. Then,
these trajectories were grouped into four clusters, i.e., Cluster1 from the north, Cluster2 from the
southwest, Cluster3 from the northeast, and Cluster4 from the east. The trajectories of each cluster
accounted for 12.6, 6.2, 58.4, and 22.8 % of total air parcels trajectories during the whole campaign,
respectively.

3. Results and discuss

3.1 Overview of meteorology and PM$_{2.5}$ chemical composition

The temporal variation of meteorological parameters, concentrations of gaseous pollutants, and
chemical compositions of PM$_{2.5}$ over the whole campaign are illustrated in Fig. 2. The missing data
were due to the acquisition software malfunction of the instrument. During the campaign, the
temperature ranged from -1.9 to 16.3 ℃ with a mean value of 7.3 ±2.8 ℃, and the RH ranged from
35 to 100 % with an average of 81 ±12.4%. The wind from the southwest prevailed with an average
speed of 0.7 ± 0.5 m/s during the entire campaign. This indicated that the atmosphere was in a
stagnant state with relatively low temperature and high RH.

The mass concentration of NR-PM$_{2.5}$ during the campaign ranged from 23 to 230 μg/m^3, with
an average of 98.5 ± 38.7 μg/m^3. This was comparable to the average PM$_{2.5}$ concentrations during
wintertime in other cities in the SCB (Table S1). The OA concentration varied from several to 103
μg/m^3, with an average of 39.2 ± 3.9 μg/m^3, constituting the majority of PM$_{2.5}$. OA contributed ~20-
69 % to PM$_{2.5}$ with an average of 40.3 ±7.6 %. The average concentrations of nitrate, sulphate,
ammonium and chloride were 29 ± 14 (ranging from ~4 to 80 μg/m^3), 10 ±4.2 (ranging from ~2 to
28 μg/m^3), 15.1 ± 6.4 (ranging from ~3 to 38 μg/m^3) and 5.2 ±4.1 μg/m^3 (ranging from ~1 to 50
μg/m^3), taking up 28.8 ± 5.5, 10.6 ±2.8, 15.3 ±2.2 and 5.1 ±3.1 % of PM$_{2.5}$, respectively. The

243 dominance of organic species was similar to previous observations in urban Chengdu during the

244 winter of 2014 and 2015 (Kong et al., 2020; Wang et al., 2018). However, the nitrate concentration

245 was higher than that of sulphate, which was contrary to that reported previously. A recent

246 observation in urban Chengdu also found that higher fraction of nitrate in $PM_{2.5}$ compared to

247 sulphate, probably due to the remarkable decrease in SO_2 emission in the past ten years (Huang et

248 al., 2021; Fu et al., 2017).

3.2 Characteristics of inorganic aerosol

250 The correlation between the molar equivalent concentrations of measured ammonium and the

251 sum of molar equivalent concentrations of nitrate, sulphate and chloride was illustrated in Fig. 3.

252 The slope of the regression line for ammonium against the sum of nitrate, sulphate and chloride with

253 a value of 1.01 indicated that the anions in $PM_{2.5}$ were well neutralised by cation (ammonium). This

254 result illustrated that nitrate, sulphate, and chloride were mainly in the form of NH_4NO_3, $(NH_4)_2SO_4$

255 and NH_4Cl, which were commonly considered secondarily formed (Ianniello et al., 2011; Ge et al.,

256 2017).

257 As SO_4^{2-} competed with NO_3^- for NH_4^+ during their formation, the relationship between nitrate-

258 to-sulphate molar ratio ($[NO_3^-]/[SO_4^{2-}]$) and ammonium-to-sulphate molar ratio ($[NH_4^+]/[SO_4^{2-}]$)

259 was indicative of the pathway of nitrate formation (He et al., 2012). If $[NO_3^-]/[SO_4^{2-}]$ linearly

260 correlated with $[NH_4^+]/[SO_4^{2-}]$ under ammonium-rich conditions ($[NO_3^-]/[SO_4^{2-}] \geq 1.5$), the

261 homogeneous formation of nitrate was expected:

262 $$HNO_3\ (g) + NH_3\ (g) \leftrightarrow NH_4NO_3\ (s, aq) \quad (1)$$
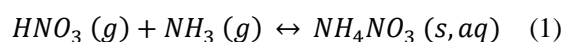
263 While for ammonium-poor conditions ($[NO_3^-]/[SO_4^{2-}] < 1.5$), the high concentration of nitrate

264 was attributed to its formation through hydrolysis of N_2O_5 on the pre-existing aerosols (Pathak et

265 al., 2009):

266 $$N_2O_5\ (aq) + H_2O\ (aq) \leftrightarrow 2NO_3^-\ (aq) + 2H^+\ (aq) \quad (2)$$
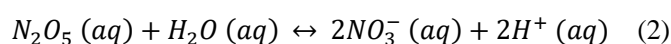
267 To better elucidate the factors affecting nitrate formation, we divided the observation period

268 into daytime (6:00 - 18:00, local time) and nighttime (18:00 - 6:00 next day, local time) hours. Fig.

269 S1 showed that the $[NO_3^-]/[SO_4^{2-}]$ during daytime was larger than 1.5, indicating ammonium-rich

270 conditions. $[NO_3^-]/[SO_4^{2-}]$ was significantly correlated with $[NH_4^+]/[SO_4^{2-}]$ during daytime with the

271 regression function:

$$\frac{NO_3^-}{SO_4^{2-}} = 0.69 \times \frac{NH_4^+}{SO_4^{2-}} - 1.08 \quad (3)$$

273   The intercept of the regression line on the $[NH_4^+]/[SO_4^{2-}]$ axis was 1.56, which was close to

274 1.5, as suggested by Pathak et al. (2009), implying that the nitrate formation was mainly driven by

275 the homogeneous pathway (Sun et al., 2011). Indeed, the nitrate concentration and nitrogen

276 oxidation ratio (NOR = $n(NO_3^-)/[n(NO_2) + n(NO_3^-)]$) increased as the Ox concentration increased

277 (as shown in Fig. 4), and exhibited a strong O_3/Ox ratio dependency, which further demonstrated

278 the homogeneous daytime formation of nitrate.

279   The emission of NOx and SO_2 had been reduced while NH_3 increased in the past almost ten

280 years, which resulted in the ammonium-rich condition in the atmosphere (Fu et al., 2017; Liu et al.,

281 2018). Despite this, a recent study showed that the nocturnal nitrate formation was not sensitive to

282 NH_3, and even increased slightly as NH_3 decreased, which was likely due to the aerosol acidity

283 effects on the partitioning of nitrate (Wen et al., 2018). Thus, the fitting of $[NO_3^-]/[SO_4^{2-}]$ vs.

284 $[NH_4^+]/[SO_4^{2-}]$ might not be applicable for identifying the nitrate formation process during

285 nighttime. The average O_3 concentration was 13.7 μg/m^3 and the average RH was 83.3 % during

286 nighttime, which favoured the aqueous-phase reactions to occur. Higher nitrate concentration was

287 observed with increasing ALWC during nighttime (as illustrated in Fig. S2), and so was NOR. This

288 phenomenon further implies the heterogeneous hydrolysis of N_2O_5 might dominate the formation

289 of nocturnal nitrate. The results were consistent with the study of Tian et al. (2019), which showed

290 that heterogeneous hydrolysis of N_2O_5 dominated nitrate formation during nighttime, while

291 photochemical reactions also played an important role in nitrate formation during daytime in two

292 megacities in Sichuan Basin.

293   Fig. S2(a) showed that the average sulphate concentration increased slightly when Ox > 60

294 μg/m^3 during daytime hours, suggesting the contribution of the photochemical process to sulphate

295 formation. However, the overall sulphur oxidation ratio (SOR = $n(SO_4^{2-})/[n(SO_2) + n(SO_4^{2-})]$)

296 decreased with increasing Ox (Fig. 4(b)), suggesting the photooxidation was not efficient for

297 converting SO_2 to sulphate. By contrast, SOR showed an increasing trend as ALWC increased,

298 demonstrating the efficient conversion of SO_2 to sulphate through aqueous-phase reactions. A

299 previous study showed that the aqueous oxidation of SO_2 by NO_2 is key to efficient sulphate

300 formation on fine aerosols with high relative humidity and NH_3 neutralisation (Wang et al., 2016).

301 As mentioned above, the atmospheric aerosols were well neutralised, and RH was high, which

302 favoured the following reaction to occur:

303 $$SO_2\ (g) + 2NO_2\ (g) + 2H_2O\ (aq) \rightarrow 2H^+(aq) + SO_4^{2-}(aq) + 2HONO(g) \quad (5)$$
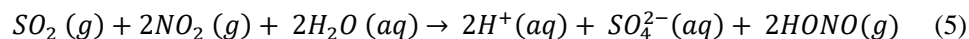
3.3 Characteristics of organic aerosol

3.3.1 Source appointment of OA

306 PMF analysis was performed to explore the OA sources measured during the whole campaign.

307 A three-factor solution was chosen as the best PMF analysis results based on the mass spectra profile,

308 variation of Q/Qexp, diurnal variation and correlation with external tracers. The resolved factors

309 included a hydrocarbon-like OA (HOA), a biomass burning OA (BBOA) and an oxygenated OA

310 (OOA). The mass spectra profiles of these three factors were shown in Fig. 5, and the temporal

311 profile of each factor and its external tracer were also shown.

312 The mass spectrum of HOA was dominated by the ions of m/z 29, 41, 55, 57, 69 and 71. HOA

313 was well correlated with BC (r = 0.77), which was largely emitted by vehicles. The diurnal cycles

314 of HOA showed two peaks during typical rush hours, demonstrating the contribution of traffic

315 emissions to HOA (Lanz et al., 2007; Zhang et al., 2005). The average concentration of HOA was

316 8.9 ± 6.5 μg/m^3 and constituted 24.2 ± 10.4 % of OA over the whole campaign. The increased

317 fraction of HOA as a function of total OA (Fig. 6) demonstrated the contribution of motor vehicle

318 emissions to haze formation.

319 BBOA was characterised by the pronounced peaks at m/z 60 (mainly $C_2H_4O_2^+$) and 73

320 $(C_3H_5O_2^+)$, which were generally regarded as biomass burning markers from levoglucosan

321 compounds (Mohr et al., 2012; Weimer et al., 2008; Alfarra et al., 2007). BBOA was well correlated

322 with m/z 60 and m/z 73 (r = 0.76 and 0.94, respectively) and accounted for 88 % of m/z 60 and 70 %

323 for m/z 73, which were higher than those in other sources. A good correlation was also found

324 between BBOA and chloride (r = 0.64), which was also suggested to be one of the tracers of biomass

325 burning. The diurnal variation of BBOA showed a similar trend of chloride (Fig. S3(a)), with two

326 peaks during 8:00-10:00 and at 19:00, which was due to the residential cooking and heating using

327 biomass. The concentration of BBOA ranged from ~1 to 34 μg/m^3, with an average of 8.9 $\pm$ 5.4

328 μg/m^3. BBOA took up 24.2 $\pm$ 8.6 % with a maximum of 46 % of OA, and its fraction also increased

329 with increasing total OA concentration, indicating the contributions of biomass burning activities

330 during haze episodes.

331   OOA was featured by the dominant signal intensities at m/z 28 (mainly CO$^+$) and m/z 44 (CO$_2^+$).

332 OOA accounted for 69 % of m/z 44, which was higher than those in other sources. The time series

333 of OOA correlated well with those of nitrate and sulphate (r = 0.81 and 0.72, respectively),

334 suggesting the commonly regional and aged properties of OOA. The concentration of OOA

335 accumulated gradually from 8:00 to 13:00, then decreased till night time. The diurnal cycle of OOA

336 was similar to solar radiation (as shown in Fig. S3(d)), suggesting OOA formation was associated

337 with photochemical reactions. The average OOA concentration showed increasing trends as Ox

338 concentration increased during both daytime and nighttime (Fig. S5), indicating the probable

339 formation pathways of OOA from its precursors (Kuang et al., 2020; Zhan et al., 2021). Note that

340 the accumulation of NO$_2$ would lead to the decrease of O$_3$/Ox ratio at night; thus, Ox might not be

341 an appropriate indicator of photochemical oxidation (Xu et al., 2017; Herndon et al., 2008). The

342 OOA formation might be attributed to other processes during nighttime. For example, previous

343 studies showed that high NOx concentration facilitated the formation of nitrate radical (NO$_3$), and

344 the NO$_3$ oxidation of biogenic volatile organic compounds (BVOC) was important for nighttime

345 secondary organic aerosol formation (Boyd et al., 2017; Rollins et al., 2012).   Except that the

346 average OOA concentration showed an increasing trend when ALWC < 200 μg/m^3 during nighttime,

347 OOA concentration did not change significantly with increasing ALWC during both day- and

348 nighttime, suggesting the aqueous-phase reactions were not a significant pathway toward OOA

349 formation.

350 **3.3.2 Elemental composition of OA**

351   The f44 vs. f43 and f44 vs. f60 during the entire campaign were illustrated in Fig. 7. The triangle

352 plot of f44 vs. f43 has been widely used to characterise OA evolution in the atmosphere because

353 m/z's 44 and 43 are usually from different functional groups, and the ratio changes as a function of

354 atmospheric aging. The f43 ranged from ~0.06 to 0.12 with an average of 0.08 $\pm$ 0.009, and the

355 range of $f44$ was ~0.07-0.24 with an average of 0.15 ±0.03, suggesting the existence of both fresh

356 and aged aerosols in the atmosphere. Most of the data were within the triangle space characterised

357 by a series of field observations and experimental data (Ng et al., 2011). However, those points with

358 higher $f44$ were outside the upper boundary of the triangle region, suggesting the corresponding

359 aerosols were more oxidised. It could be observed that the points with higher $f44$ (> 0.16)

360 corresponded to relatively higher Ox concentration and lower ALWC, while those with lower $f44$

361 corresponded to relatively lower Ox concentration and higher ALWC, suggesting that the formation

362 of more oxidised OOA was mainly attributed to photochemical reactions, and the formation of less

363 oxidised OOA was probably attributed to aqueous-phase reactions (Zhao et al., 2019; Kim et al.,

364 2019).

365   The triangle plot of $f44$ vs. $f60$ was widely used as a metric to access the evolution of

366 atmospheric BBOA (Cubison et al., 2011). A value of 0.003 for $f60$ was recommended as an

367 appropriate value to represent the atmospheric background free of biomass burning influence (Aiken

368 et al., 2009; Docherty et al., 2008). The $f60$ ranged from 0.0028 to 0.055 with an average of 0.008

369 ±0.003 during the campaign. Except for several points, the $f60$ was ubiquitously higher than 0.003

370 and most points fell in the triangular region, suggesting the contribution of biomass burning to OA.

371 The $f44$ and $f60$ of BBOA resolved by PMF in the present study were also in the triangular region

372 and comparable with previous studies (Paglione et al., 2020; Zhao et al., 2019; Kim et al., 2019).

373 Fig. S6 showed that $f44$ increased while $f60$ decreased with increasing Ox, indicating the likely

374 oxidation of levoglucosan and/or levoglucosan-like substances. Cubison et al. (2011) suggested that

375 the increasing $f44$ was not only attributed to the oxidation of levoglucosan-like species, but the

376 oxidation of bulk OA also played a role because the levoglucosan-like species only contributed a

377 small fraction of the OA mass (Aiken et al., 2009). Their contribution to the total signal m/z 44

378 before or after aging was also small. Compared to the effects of Ox, the increasing ALWC did not

379 seem to push $f60$ to the left upper region. Most of the data points, which corresponded to high

380 ALWC, were within the region of aged BBOA in the $f44$ vs. $f60$ space as defined previously by

381 Paglione et al. (2020), indicating the probable aqueous-phase oxidation of BBOA. Although the

382 aqueous OOA (aq-OOA) could not be resolved in the present study, we deduced that the aqueous-

383 phase reactions occurred and contributed to the formation of OOA, for (1) the ambient RH was

384 typically above 65%, which favoured the presence of wet aerosol particles; (2) the range of O/C

14

385   estimated from the Improved-Ambient (IA) method varied from 0.46 to 0.85 when the ambient RH >

386   80 %, covering the O/C range of the OOA obtained from the photooxidation of organic precursors

387   in the aqueous phase and ambient aq-OOA observed in many other cities (Duan et al., 2021;

388   Mandariya et al., 2019; Sun et al., 2010; Xu et al., 2017; Gilardoni et al., 2016).

389   The evolution of OA during the whole campaign was characterised by the van Krevelen (VK)

390   diagram in Fig. 8. The slope obtained from the linear regression of H:C versus O:C plotted in the

391   VK-$\overline{OS_c}$ space could be used to infer the composition of OA and the chemical process in OA

392   formation (Docherty et al., 2018). The slope of 0 in VK-$\overline{OS_c}$ plot was related to the replacement of

393   a hydrogen atom with an OH moiety, while the slopes of -0.5 and -1 indicated the formation of

394   carboxylic groups with/without fragmentation, and a slope of -2 was equivalent to the replacement

395   of an aliphatic carbon with a carbonyl group (Heald et al., 2010; Ng et al., 2011). The slope of the

396   linear fitting line for all the data points was -0.14, suggesting the probable formation of carboxylic

397   acid moieties and hydroxyl groups. The slopes of the linear fitting lines for each fog episode were similar

398   and close to zero, which was consistent with the hydroxyl group formation possibly taking place in

399   aerosol water through dark chemistry (Sun et al., 2010; Yu et al., 2014; Zhao et al., 2014).

3.4 Regional transport

401   Air parcels from the north (Cluster1) transported at relatively high heights before arriving at

402   the observation site (as illustrated in Fig. 9), and corresponded to the lowest average $PM_{2.5}$

403   concentration (66 ± 30 μg/m^3). The air parcels of Clsuter2 had the longest transport distance and

404   highest transport height. Although they took up the least proportion of total air parcels, they had the

405   highest average $PM_{2.5}$ concentration (119 ± 30 μg/m^3) during the whole campaign, suggesting that

406   pollutants accumulated high in the air. Air parcels from the east (Cluster3) with the shortest transport

407   distance and relatively low transport height had an average $PM_{2.5}$ concentration of 113 ± 34 μg/m^3.

408   This indicated that the pollutants might be brought to the observation site along with the transport

409   of air parcels originating from adjacent areas. The air parcels from the northeast of Sichuan province

410   (Cluser4) had the lowest transport height; however, the corresponding $PM_{2.5}$ concentration was

411   lower than that of Cluster3.

412   Compared to cluster1 and cluster4, a higher contribution of nitrate to $PM_{2.5}$ was observed for

413   Cluster2 and Cluster3, which was mainly related to the intense emission from industry and vehicles.

414   However, the contribution of BBOA was higher for Cluster3 and Cluster4 compared to other clusters,

415   suggesting intense biomass burning along their transport paths.

416   To better understand the potential pollutant sources during the campaign, the potential source

417   contribution function (PSCF) was applied to analyse the possible regions that might contribute to

418   haze formation. The spatial distribution of weighted PSCF for different chemical compositions was

419   illustrated in Fig. 10. The WPSCF values for organics over the southwest and southeast were > 0.7,

420   indicating these locations were likely source areas of organics. For nitrate and sulphate, the areas

421   by the southwest and south of the sampling site were potential source regions. The major source

422   regions for HOA were the areas of south and northeast Deyang. The regions contributing to BBOA

423   were the areas of east Sichuan province, which was consistent with a higher proportion of BBOA in

424    $PM_{2.5}$ in the air parcels stemming from these locations. For OOA, the WPSCF values over the

425   southwest and southeast of Deyang and northeast Sichuan province were > 0.7, suggesting the

426   contribution of these regions.

427   **3.5 Case studies for haze pollution**

428   **3.5.1 Factors driving the evolution of haze episodes**

429   As mentioned above, three haze episodes were identified over the whole campaign. The

430   synoptic conditions and aerosol chemical composition for each haze episode were summarised in

431   Table. S3. The average temperature during H2 was lower than those during H1 and H3, while the

432   average solar radiation was higher. The mean RH and wind speed were almost the same during each

433   haze episode. The average concentrations of aerosol chemical composition and their contributions

434   to $PM_{2.5}$ were different in each haze episode, indicating that the factors causing haze formation

435   might be different during the campaign.

436   The average $PM_{2.5}$ concentrations measured by ToF-ACSM during H1, H2, and H3 were 113

437   ±46, 109 ±46, and 104 ± 30 μg/m³, respectively. The average mass fractions of OA, nitrate, sulphate,

438   ammonium, and chloride were similar during H1 and H3 (as shown in Fig. 11(a)). During H2, the

439   mass fractions of sulphate and ammonium were slightly higher than those in H1 and H3, while the

440   mass fractions of OA and chloride were lower. In OA, the fraction of primary organic aerosols (POA

16

441 = HOA + BBOA) during H3 was higher than those during H1 and H2. The fraction of BBOA showed

442 an increasing trend from H1 to H3, demonstrating the contribution of biomass burning to haze

443 formation. Despite the importance of BBOA to winter haze formation in SCB, the control of biomass

444 burning did not receive much attention, and more efforts were needed for atmospheric aerosol

445 mitigation in the future.

446   Fig. 11(b) showed that the concentrations of OA, nitrate, sulphate, ammonium, and chloride

447 all increased as the ambient air quality worsened (implying by the increasing $PM_{2.5}$ concentration)

448 during each haze episode. During H1, the fraction of nitrate in $PM_{2.5}$ increased, while the proportions

449 of sulphate, OOA, and HOA in $PM_{2.5}$ decreased as the $PM_{2.5}$ concentration increased, indicating the

450 evolution of this haze episode was mainly driven by the reactions involving nitrate formation. The

451 average NO_3^- formation rate as a function of $PM_{2.5}$ concentration during H1 was depicted in Fig. S7.

452 The NO_3^- formation rate increased fast as $PM_{2.5}$ concentration increased from 50 to 110 $\mu g/m^3$,

453 which also showed the rapid formation of nitrate contributed to haze formation. In contrast, the

454 average nitrate formation rates were below zero when the $PM_{2.5}$ concentration was < 130 $\mu g/m^3$

455 during H2 and H3, suggesting nitrate formation did not play an important role at the early stage of

456 H2 and H3. Although the nitrate formation rate decreased when $PM_{2.5}$ concentration was > 110

457 $\mu g/m^3$ during H1, it remained positive, suggesting the nitrate concentration increased gradually.

458   For H2, the fraction of nitrate and ammonium in $PM_{2.5}$ did not show apparent changes, and the

459 fractions of sulphate and OOA decreased, while the fractions of BBOA and HOA increased as the

460 air quality worsened, demonstrating that the emission of primary organic aerosols from biomass

461 burning and vehicle exhaust were the major factors which drove the haze formation. During H3, the

462 fractions of nitrate and BBOA in $PM_{2.5}$ increased, while OOA decreased and the rest composition

463 did not change significantly as the $PM_{2.5}$ concentration increased, showing that the evolution of this

464 haze episode was mainly driven by the reactions involving nitrate formation and biomass burning.

465 The fire maps (as illustrated in Fig. S8) showed that more fire spots during H2 and H3 were observed

466 around Deyang compared to non-haze episodes, suggesting the biomass burning activities were

467 more intensive during these haze episodes.

468   The average estimated O:C and H:C during H1 and H2 were similar and slightly higher/lower

469 than that during H3, thus resulting in a higher carbon oxidation state ($\overline{OS_c} \approx 2O:C - H:C$) during

470 H1 and H2. The lower average $\overline{OS_c}$ during H3 might be due to the higher proportion of HOA and

471   BBOA, which did not undergo long-time aging and kept relatively fresh in the atmosphere.

472   **3.5.2 Evolution of chemical composition during fog periods**

473   The fog periods usually started at night or early morning and dissipated in the afternoon. The

474   individual meteorological parameter differed among each fog period (as summarised in Table S3).

475   The average temperature was the highest during F1 (6.2 $\pm$ 2.3 ℃), and the lowest was observed

476   during F2 (1.5 $\pm$ 3.2 ℃). The maximum solar radiation during F1 and F2 (470 and 500 W/m^2) were

477   similar and much higher than that during F3 (75 W/m^2). The synoptic conditions with low

478   temperature and calm wind favoured the formation of radiation fogs in each fog period.

479   The chemical composition of PM$_{2.5}$ was also different during each fog period. The average

480   concentrations of organics, nitrate, and ammonium were almost the same during F2 and F3 and

481   significantly lower than those during F1. However, the average chloride concentration during F2

482   was twice of those during F1 and F3, suggesting the possibility of stronger biomass burning

483   emissions during F2. OOA constituted the major part of OA during F1, while HOA and BBOA were

484   more important than OOA during F2 and F3. The domination of secondary species in PM$_{2.5}$ during

485   F1 was probably due to the aqueous-phase reaction, while the primary emission tended to be

486   stronger during F2 and F3.

487   Since the aerosols were dried by a Nafion drier, the aerosols that ToF-ACSM measured were

488   the interstitial particles in droplets or those excluded from fog droplets. In order to better characterise

489   the evolution of chemical composition in each fog period, the intervals for 3 h before and after the

490   fog period, when ambient RH was lower than 95 %, were regarded as pre-fog and post-fog periods,

491   respectively (Kim et al., 2019). Note that the post-fog was not assigned for F3 because the ToF-

492   ACSM data were not available with a failure of acquisition software.

493   The average concentrations of different chemical compositions during the evolution of fog

494   episodes (pre-fog, during fog, and post-fog) were illustrated in Fig. 12. Compared to the pre-fog

495   period of F1, all species in the interstitial aerosols decreased during the foggy period, likely due to

496   the scavenging by fog droplets. Note that the OOA and sulphate decreased less than other species,

497   probably due to the OOA and sulphate formation through aqueous-phase reactions against the

498   scavenging effect of fog droplets. Except for OOA and nitrate, all species kept decreasing during

499 post-fog periods, which might be attributed to the increase of the planet boundary layer (PBL) height.

500 The increase of OOA and nitrate was probably associated with the enhancement of photochemical

501 reaction after the dissipation of fog.

502   Distinguished from F1, all species (except for HOA) increased during the foggy period from

503 the pre-fog period during F2. Although hydrophilic species (e.g., nitrate, sulphate, and OOA) tended

504 to be scavenged by fog droplets, it seemed that the formation of OOA, nitrate, sulphate, and

505 ammonium was significantly faster than wet removal, thus resulting in an increase during the foggy

506 period. BBOA and HOA were commonly considered as hydrophobic species, and they were

507 excluded from fog droplets. Previous studies showed that BBOA and HOA concentrations decreased

508 during the foggy period compared to the pre-fog period (Collett et al., 2008; Kim et al., 2019),

509 despite their insoluble nature. The increase of BBOA in the present study was attributed to the

510 intense emission from biomass burning during the foggy period, which overwhelmed the scavenging

511 effects of fog droplets. During the post-fog period, BBOA and HOA decreased significantly,

512 possibly due to weaker emission and the efficient removal of fog droplets through nucleation and/or

513 coagulation. The dynamics of PBL might also play a role because the temperature kept increasing,

514 and higher PBL was expected during the post-fog period. With stronger solar radiation, OOA, nitrate,

515 and ammonium continued growing during the post-fog period from the foggy period through

516 photochemical reactions. However, sulphate slightly decreased, which might be due to the

517 insufficient formation through photochemical reactions, and decreased as the PBL height increased.

518 Similar to F2, all the secondary species increased during the foggy period from the pre-fog period

519 during F3. However, BBOA and HOA were reduced significantly by the scavenging of fog droplets.

520   The average elemental O:C showed an increasing trend from pre-fog periods to post-fog/foggy

521 periods, while H:C did not change significantly for different fog events, suggesting the OA became

522 more oxidised. As shown in Fig. S9, the mass fractions of OOA increased, while the contribution of

523 BBOA and HOA decreased from pre-fog periods to post-fog/foggy periods for the three fog events.

524 As a consequence, the O:C increased in line with the increased contribution of OOA. Previous

525 studies had reported that the aqueous-phase reactions enhanced OOA formation during fog/high RH

526 periods (Chakraborty et al., 2016; Kuang et al., 2020; Chakraborty et al., 2015). It appeared that the

527 OOA formation would balance out the scavenging of fog droplets during the foggy period for the

528 three fog events, despite the hydrophilic OOA being preferentially scavenged by fog droplets. Thus,

529   the OOA concentration marginally decreased or even increased during foggy periods.

530   **4. Conclusions**

531   Haze pollution has long been a severe environmental problem in SCB. The formation process

532   of haze pollution in SCB might be different from those in NCP, YRD, and PRD due to the unique

533   topography and meteorological conditions, which are still unclear. Based on the measurement data

534   of a ToF-ACSM and combined with the PMF and PSCF analysis, the temporal variation, formation

535   process, and sources of $PM_{2.5}$ were characterised to elucidate further the factors contributing to haze

536   formation. It was found that the concentrations of OA and nitrate increased dramatically as $PM_{2.5}$

537   concentration increased, and the stagnant synoptic condition favoured the accumulation of these

538   pollutants. For different haze events, the driving factors could be classified into three types: one was

539   the reactions involving nitrate formation; another one was the intense biomass burning and vehicle

540   exhaust emissions, and the last one was the combination of the reactions involving nitrate formation

541   and biomass burning. Nitrate formation was primarily affected by photooxidation during daytime,

542   while the nocturnal nitrate formation was dominated by aqueous-phase reactions. OOA constituted

543   a major part of OA, and it was mainly generated through photooxidation, while aqueous-phase

544   reactions did not significantly promote its formation.

545   Due to the limitation of the present study, the parameters which are indicative of the pathways

546   of nitrate formation are not characterised. The major precursors contributing to a large amount of

547   OOA are not clear yet. In addition, how controlling BBOA will affect the atmospheric visibility,

548   radiative forcing, and climate change in SCB needs further investigation in the future. In spite of

549   the deficiencies, the results in this study implied that controlling primary emissions (such as biomass

550   burning and vehicle exhaust) and precursors of secondary aerosols (e.g., NOx, SO_2, and VOCs)

551   during severe haze periods will benefit the improvement of air quality in SCB.

552

553

554 *Data availability.* The data generated and analysed in this study are available on visiting

555 https://doi.org/10.5281/zenodo.6965551.

556

557 *Author contributions.* FY and SX designed this study. XZ and QL contributed to data collection

558 during the field campaign. JZ, DZ, and CZ performed field experiments. ZL and CP performed the

559 data analysis. ZB wrote the manuscript. GS, LZ, and YC contributed to the scientific discussion and

560 paper correction.

561

562 *Competing interests.* The authors declare that they have no conflict of interest.

563

569
570

571
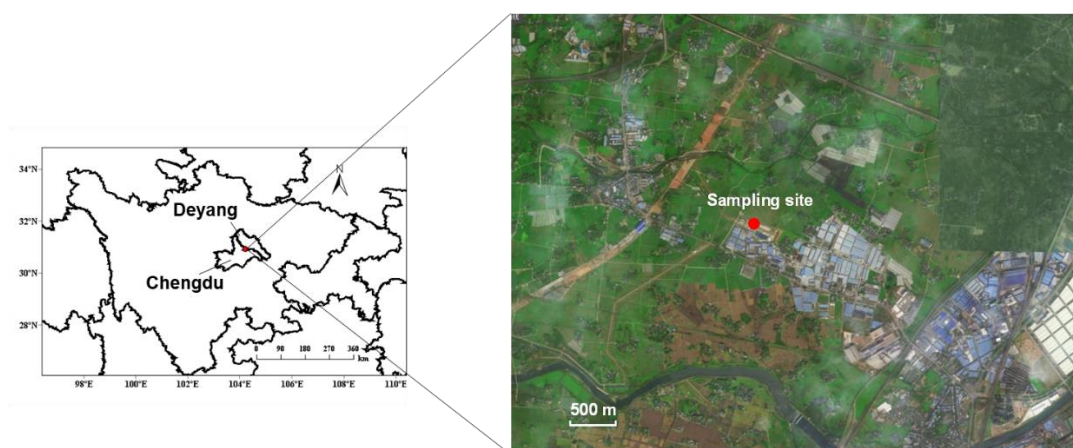
572

573   Fig. 1 Location of the observation site (from Baidu Maps, ©2022 Baidu – GS(2021)6026).

574

575

576
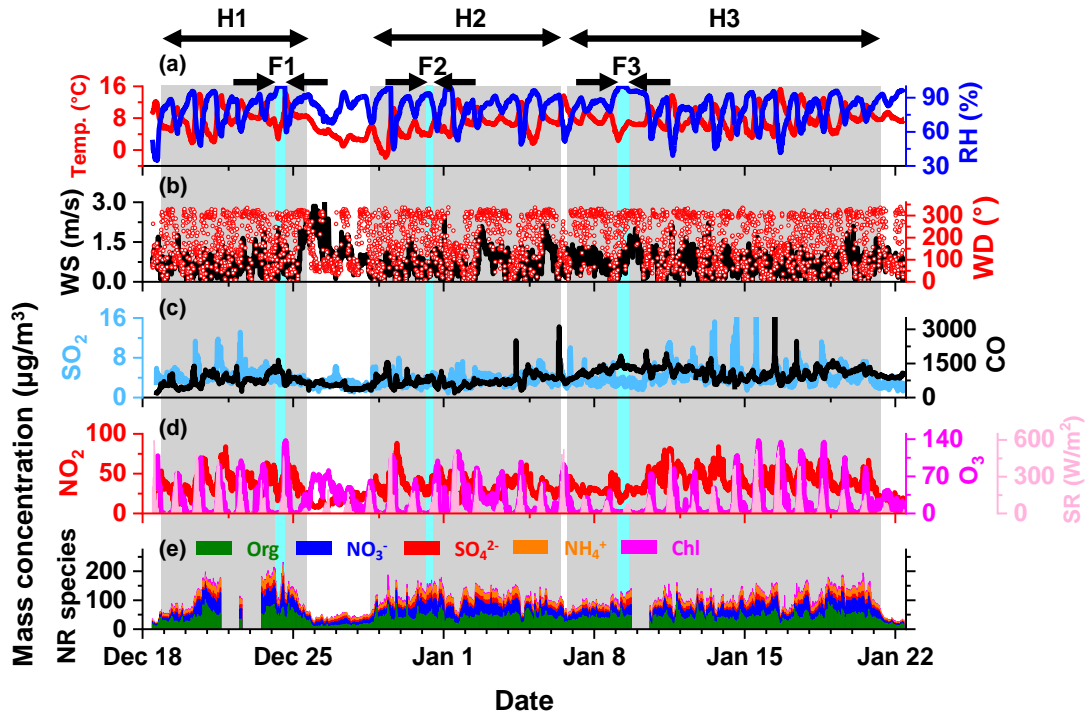
Fig. 2 Time series of (a) relative humidity (RH) and temperature (T); (b) wind direction and wind
speed; (c), (d) CO, NO_2, SO_2, and O_3 mass concentrations and solar radiation; (e) mass concentration
of organics, nitrate, sulphate, ammonium, and chloride in NR-$PM_{2.5}$. The grey-shaded areas
represent the intervals of H1, H2, and H3, respectively. The light blue-shaded areas represent the
intervals of F1, F2, and F3, respectively.

583

584
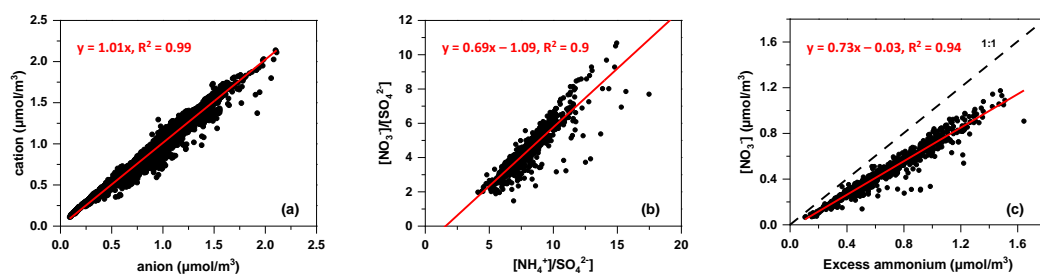
585 Fig. 3 Scatter plots of (a) molar concentrations of cations vs. anions, (b) molar ratios of nitrate to

586 sulphate vs. ammonium to sulphate, and (c) molar concentrations of nitrate vs. excess ammonium.

587

588

589

590
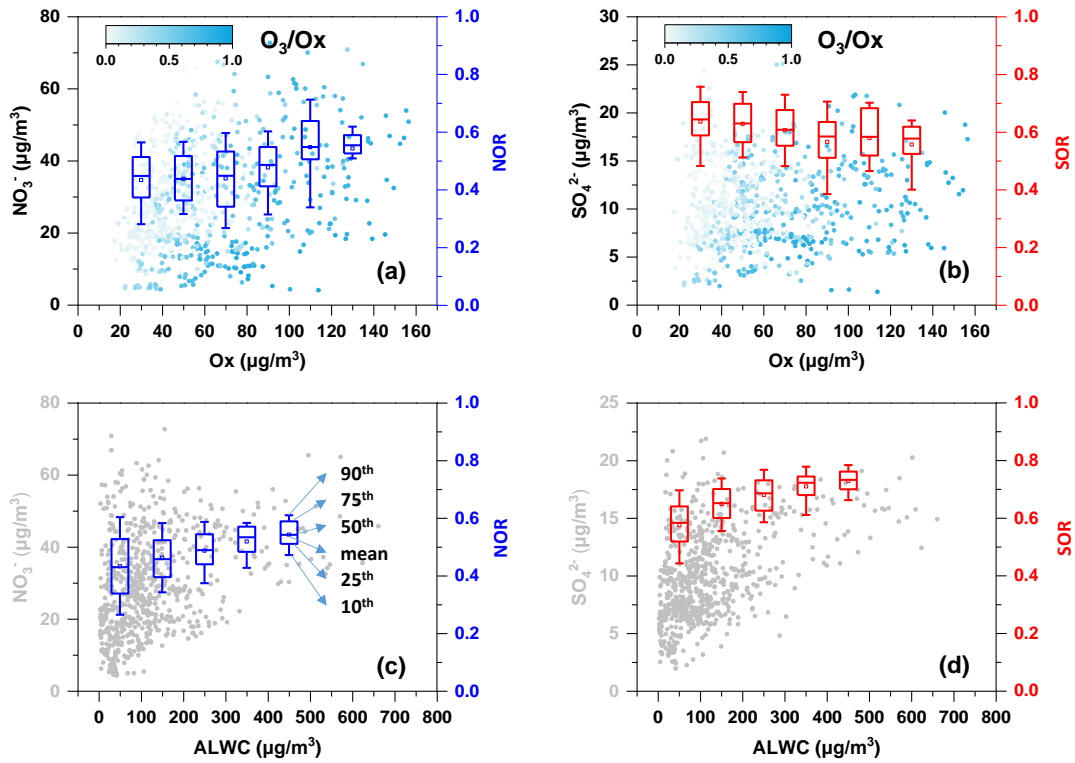
Fig. 4 Variation of (a), (c) nitrate and NOR and (b), (d) sulphate and SOR as Ox/ALWC increases.

The data NOR and SOR were grouped into different bins according to 20 μg/m³ increment of Ox in

(a) and (b), and 100 μg/m³ increment of ALWC in (c) and (d). The colour scale represents O_3/Ox

ratios in (a) and (b). The mean (square), 50th (horizontal line inside the box), 25th and 75th

percentiles (lower and upper box), and 10th and 90th percentiles (lower and upper whiskers) of the

box chart are marked in (c). The concentration of ALWC was simulated using the ISORROPIA-II model.

599

600

601
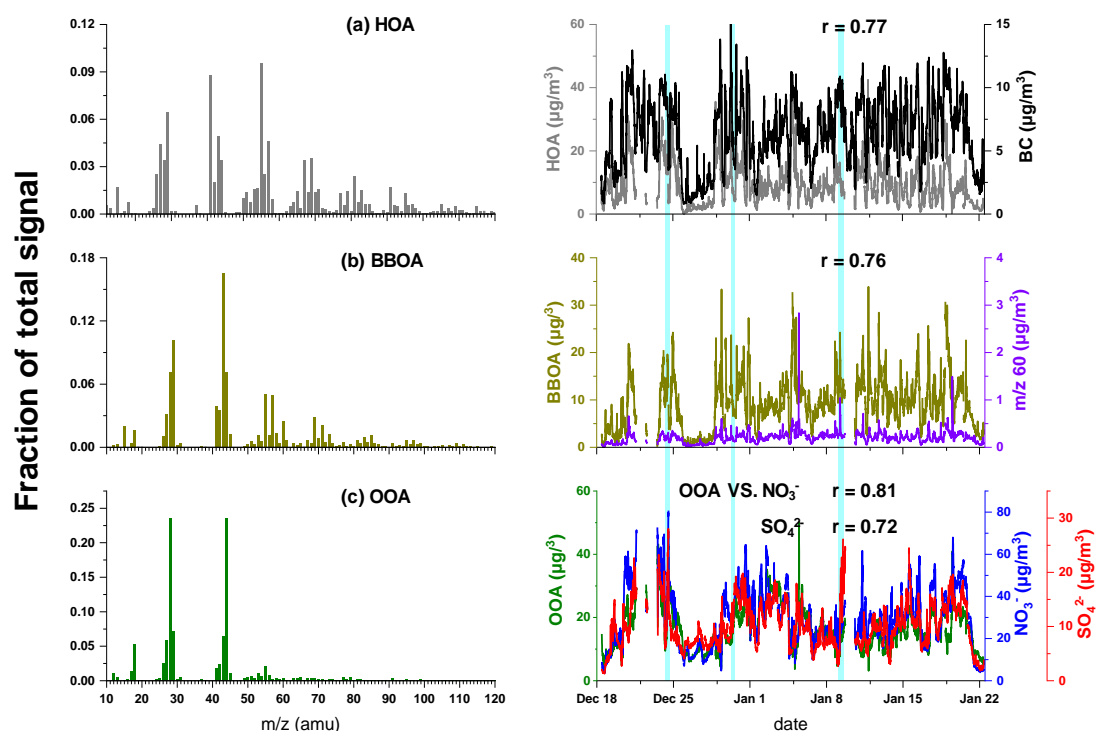
Fig. 5 Mass spectrum of (a) HOA, (b) BBOA, and (c) OOA resolved by PMF. The time series of

each OA source and corresponding tracers are depicted in the right panel. The light blue shaded

areas represent the intervals of foggy periods.
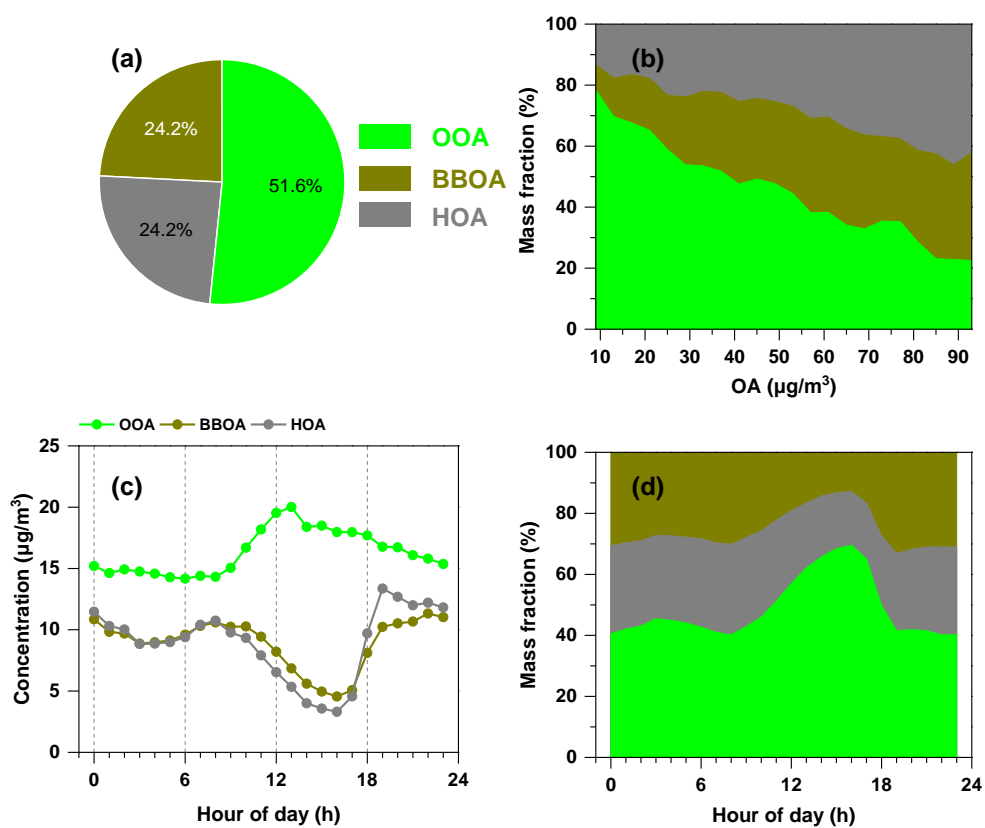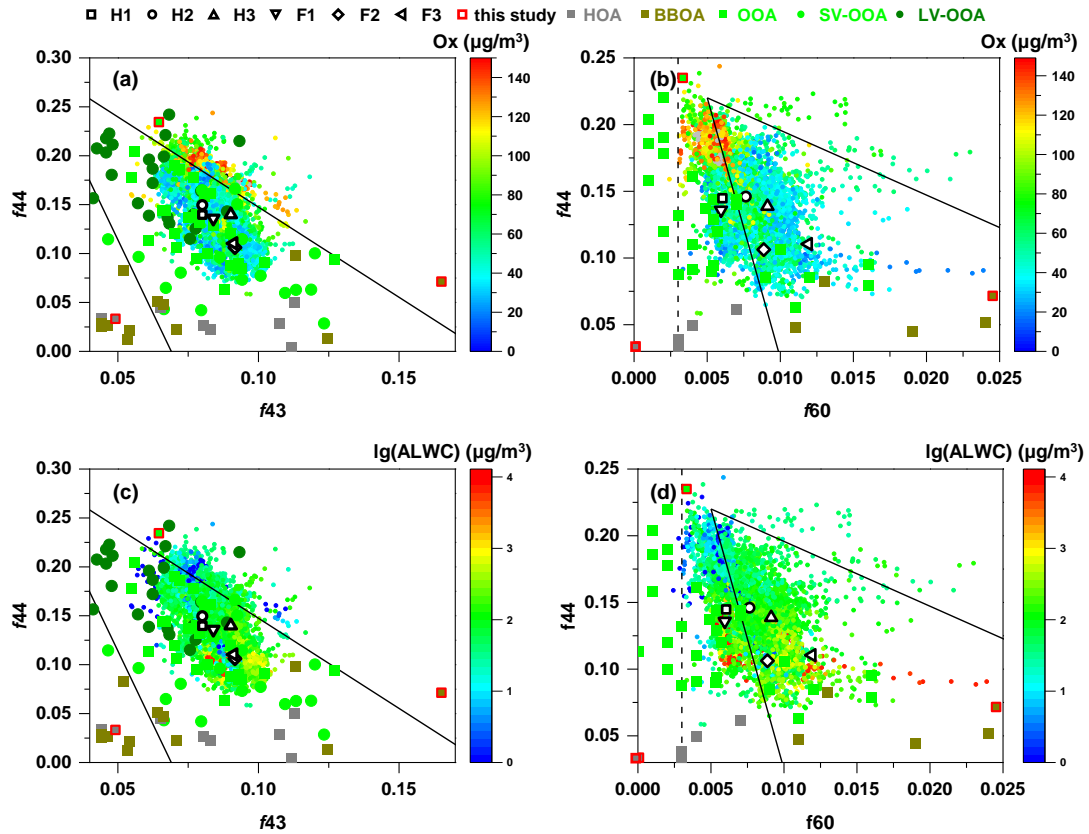
605

606

Fig. 6 Average mass fraction of different OOA, BBOA, and HOA (a) in OA and (b) as a function of OA mass concentration. The diurnal variation of different OA compositions and their mass contributions are shown in (c) and (d).

613

Fig. 7 Triangle plots of (a), (c) $f44$ (ratio of m/z 44 to total signal in the component mass spectrum) vs. $f43$ (ratio of m/z 43 to total signal in the component mass spectrum), and (b), (d) $f44$ vs. $f60$ (ratio of m/z 60 to total signal in the component mass spectrum) during the whole campaign. The colour scale in (a) and (b) represents Ox concentration, and that in (c) and (d) represents lg(ALWC). The solid lines in (a) and (c) are derived from the results reported by Ng et al. (2010). The dashed line representing the background value of secondary aged OA and the solid guidelines in (b) and (d) are derived from Cubison et al. (2011). The $f44$ vs. $f43$ and $f44$ vs. $f60$ for different OA sources reported in previous studies are also shown (Kim et al., 2019; Ng et al., 2011; Wang et al., 2016; Zhao et al., 2019; Paglione et al., 2020).
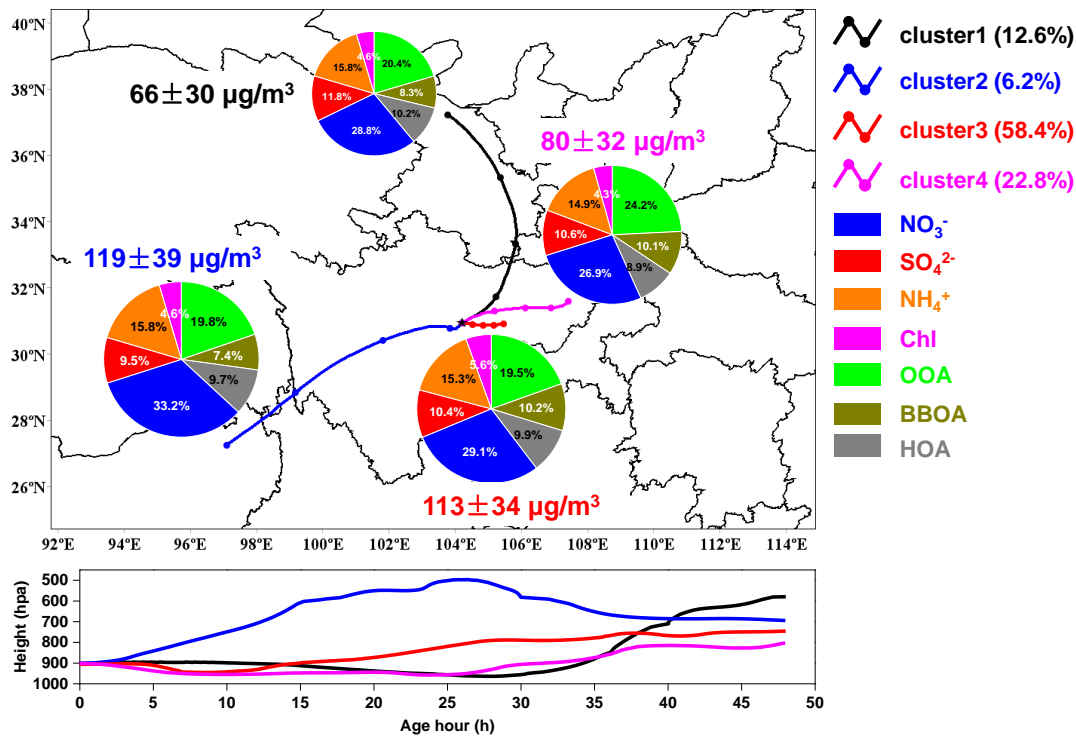
624

625

626

627
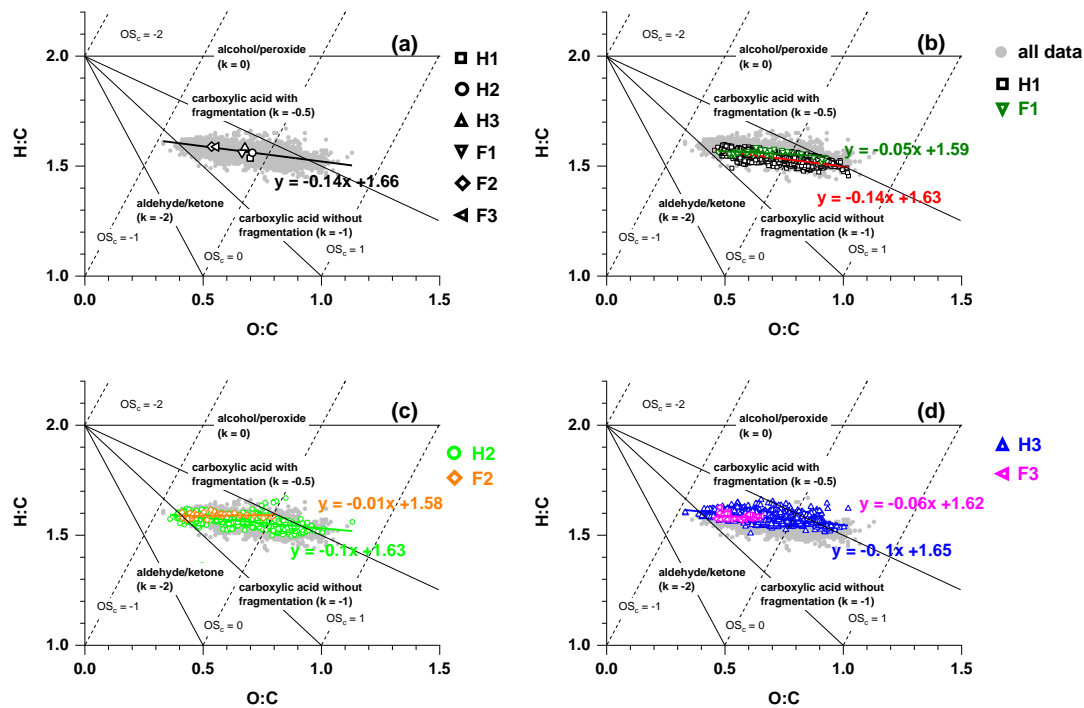
Fig. 8 The Van Krevelen-$\overline{OS_c}$ diagram with data during (a) the whole campaign, (b) H1 and F1, (c)

H2 and F2, and (d) H3 and F3. The triangle lines with different slopes show distinct formation

processes (Heald et al., 2010).

631

632

635   Fig. 9 Simulation results of 48 h backward air parcels cluster-mean trajectories during the campaign.

636   The lines in black, blue, red, and purple represent the mean trajectories of Cluster1 to Cluster4,

637   respectively. The pie charts show the average mass contribution of different chemical compositions
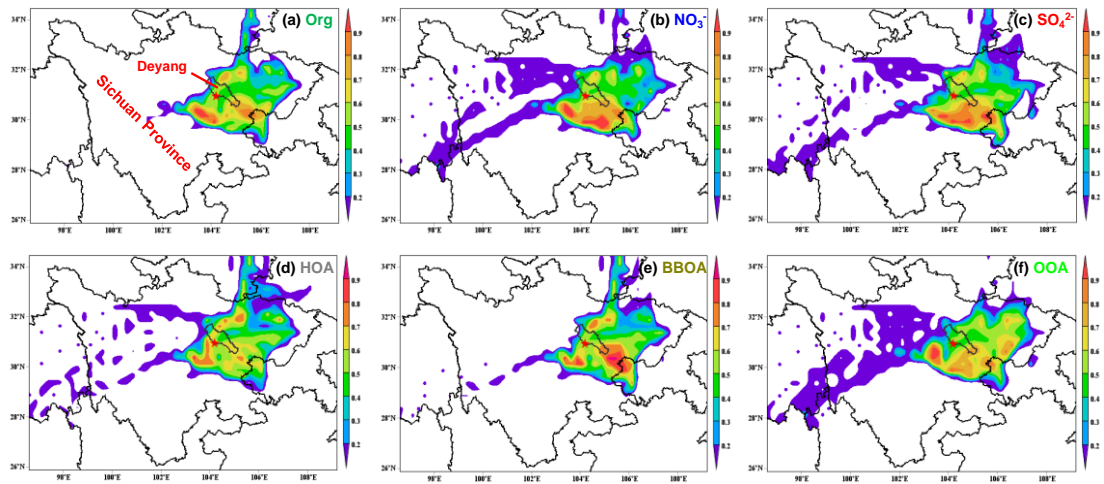
638   to PM$_{2.5}$ for each cluster. The lower panel shows the height profile for different air parcels clusters

639   along their transport paths.

640

641

642

643

Fig. 10 Simulation results of PSCF for (a) organics, (b) nitrate, (c) sulphate, (d) HOA, (e) BBOA, and (f) OOA during the whole campaign. The 50th percentile of the concentrations for each composition (organics: 39.5 μg/m^3, nitrate: 27.8 μg/m^3, sulphate: 9.5 μg/m^3, HOA: 7.6 μg/m^3, BBOA: 8.7 μg/m^3, OOA: 15.2 μg/m^3) were used as thresholds in the PSCF analysis. The areas of Deyang and Sichuan Province are marked in (a).

649

650

651

652
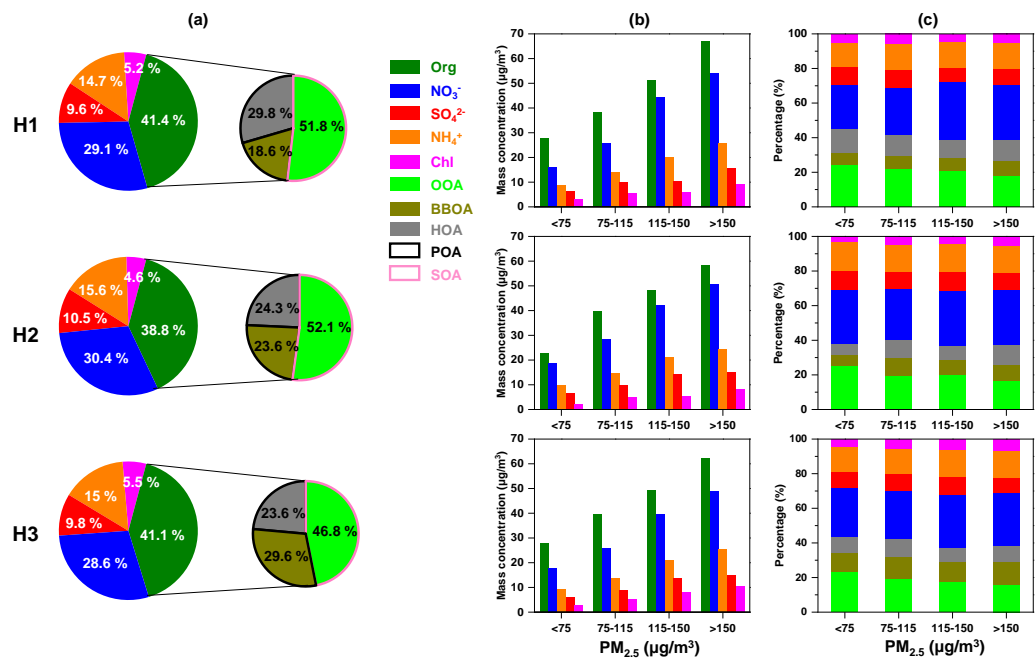
653

654 Fig. 11 (a) Average mass fractions of different chemical compositions in PM$_{2.5}$, (b) mass

655 concentration, and (c) relative contribution of inorganic/organic species as a function of PM$_{2.5}$

656 concentration during each haze episode. The right panel in (a) depicts the contribution of OOA,

657 BBOA, and HOA to OA.

658

659

660
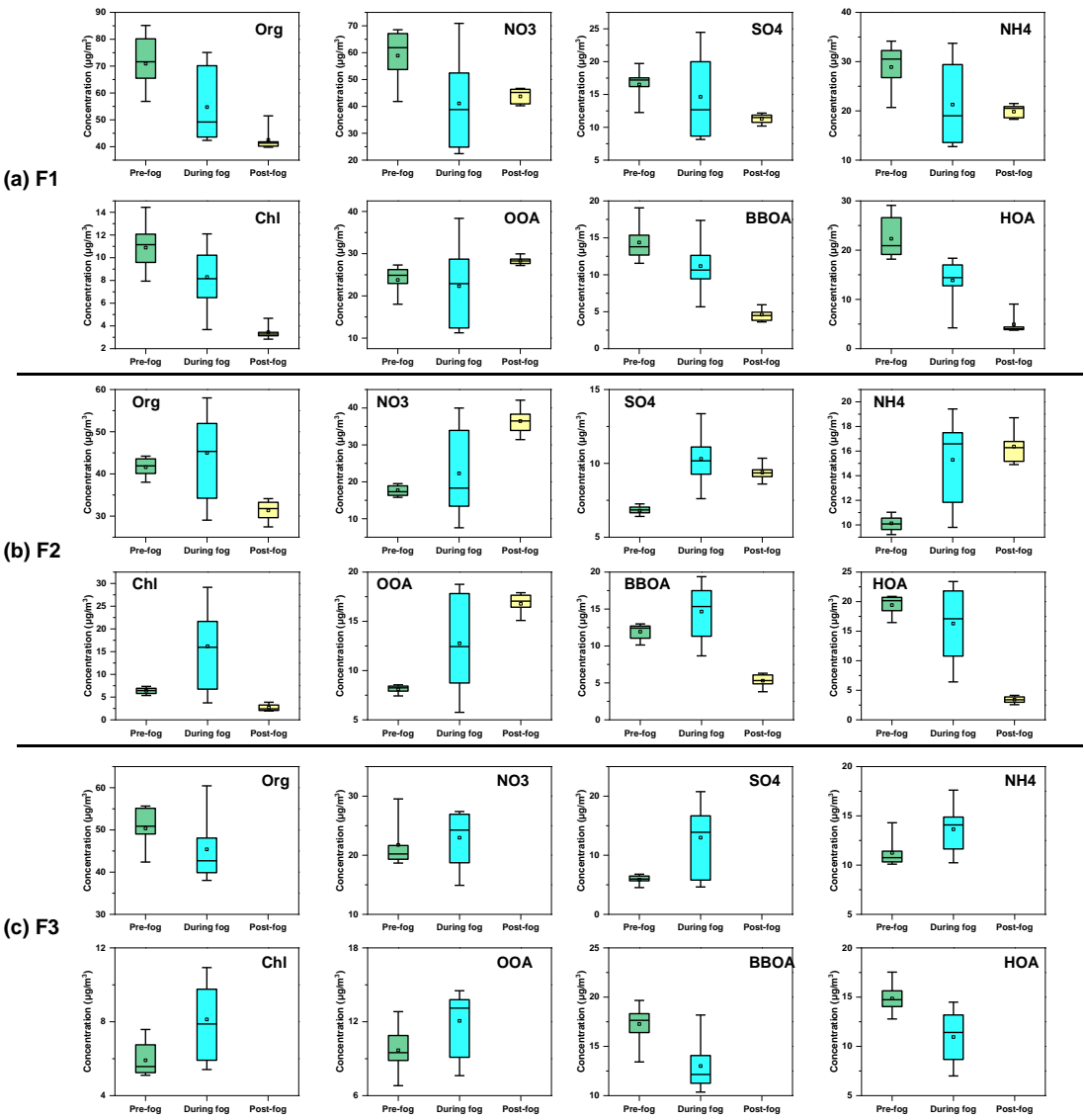
Fig. 12 Variation of organics, nitrate, sulphate, ammonium, chloride, OOA, BBOA, and HOA
concentration during the evolution of (a) F1, (b) F2, and (c) F3.

661

662

663

664

665

References

Aiken, A. C., Salcedo, D., Cubison, M. J., Huffman, J. A., DeCarlo, P. F., Ulbrich, I. M., Docherty, K. S., Sueper, D., Kimmel, J. R., Worsnop, D. R., Trimborn, A., Northway, M., Stone, E. A., Schauer, J. J., Volkamer, R. M., Fortner, E., de Foy, B., Wang, J., Laskin, A., Shutthanandan, V., Zheng, J., Zhang, R., Gaffney, J., Marley, N. A., Paredes-Miranda, G., Arnott, W. P., Molina, L. T., Sosa, G., and Jimenez, J. L.: Mexico City aerosol analysis during MILAGRO using high resolution aerosol mass spectrometry at the urban supersite (T0) – Part 1: Fine particle composition and organic source apportionment, Atmos. Chem. Phys., 6633-6653, https://doi.org/10.5194/acp-9-6633-2009, 2009.

Alfarra, M. R., Prevot, A. S. H., Szidat, S., Sandradewi, J., Weimer, S., Lanz, V. A., Schreiber, D., Mohr, M., and Baltensperger, U.: Identification of the Mass Spectral Signature of Organic Aerosols from Wood Burning Emissions, Environ. Sci. Technol., 41, 5770-5777, https://doi.org/10.1021/es062289b, 2007.

Bao, Z., Chen, L., Li, K., Han, L., Wu, X., Gao, X., Azzi, M., and Cen, K.: Meteorological and chemical impacts on PM2.5 during a haze episode in a heavily polluted basin city of eastern China, Environ. Pollut., 250, 520-529, https://doi.org/10.1016/j.envpol.2019.04.045, 2019.

Boyd, C. M., Nah, T., Xu, L., Berkemeier, T., and Ng, N. L.: Secondary Organic Aerosol (SOA) from Nitrate Radical Oxidation of Monoterpenes: Effects of Temperature, Dilution, and Humidity on Aerosol Formation, Mixing, and Evaporation, Environ. Sci. Technol., 51, 7831-7841, https://doi.org/10.1021/acs.est.7b01460, 2017.

Canagaratna, M. R., Jimenez, J. L., Kroll, J. H., Chen, Q., Kessler, S. H., Massoli, P., Hildebrandt Ruiz, L., Fortner, E., Williams, L. R., Wilson, K. R., Surratt, J. D., Donahue, N. M., Jayne, J. T., and Worsnop, D. R.: Elemental ratio measurements of organic compounds using aerosol mass spectrometry: characterization, improved calibration, and implications, Atmos. Chem. Phys., 15, 253-272, https://doi.org/10.5194/acp-15-253-2015, 2015.

Chakraborty, A., Bhattu, D., Gupta, T., Tripathi, S. N., and Canagaratna, M. R.: Real-time measurements of ambient aerosols in a polluted Indian city: Sources, characteristics, and processing of organic aerosols during foggy and nonfoggy periods, J. Geophys. Res.-Atmos., 120, 9006-9019, https://doi.org/10.1002/2015JD023419, 2015.

696 Chakraborty, A., Gupta, T., and Tripathi, S. N.: Combined effects of organic aerosol loading and fog

697   processing on organic aerosols oxidation, composition, and evolution, Sci. Total Environ., 573, 690-

698   698, https://doi.org/10.1016/j.scitotenv.2016.08.156, 2016.

699 Chen, Q., Fu, T., Hu, J., Ying, Q., and Zhang, L.: Modelling secondary organic aerosols in China, Natl.

700   Sci. Rev., 4, 806-809, https://doi.org/10.1093/nsr/nwx143, 2017.

701 Chen, Q., Heald, C. L., Jimenez, J. L., Canagaratna, M. R., Zhang, Q., He, L. Y., Huang, X. F.,

702   Campuzano Jost, P., Palm, B. B., Poulain, L., Kuwata, M., Martin, S. T., Abbatt, J. P. D., Lee, A. K.

703   Y., and Liggio, J.: Elemental composition of organic aerosol: The gap between ambient and laboratory

704   measurements, Geophys. Res. Lett., 42, 4182-4189, https://doi.org/10.1002/2015GL063693, 2015.

705 Clark, C. H., Kacarab, M., Nakao, S., Asa-Awuku, A., Sato, K., and Cocker, D. R.: Temperature Effects

706   on Secondary Organic Aerosol (SOA) from the Dark Ozonolysis and Photo-Oxidation of Isoprene,

707   Environ. Sci. Technol., 50, 5564-5571, https://doi.org/10.1021/acs.est.5b05524, 2016.

708 Collett, J. L., Herckes, P., Youngster, S., and Lee, T.: Processing of atmospheric organic matter by

709   California radiation fogs, Atmos. Res., 87, 232-241, https://doi.org/10.1016/j.atmosres.2007.11.005,

710   2008.

711 Cubison, M. J., Ortega, A. M., Hayes, P. L., Farmer, D. K., Day, D., Lechner, M. J., Brune, W. H., Apel,

712   E., Diskin, G. S., Fisher, J. A., Fuelberg, H. E., Hecobian, A., Knapp, D. J., Mikoviny, T., Riemer, D.,

713   Sachse, G. W., Sessions, W., Weber, R. J., Weinheimer, A. J., Wisthaler, A., and Jimenez, J. L.:

714   Effects of aging on organic aerosol from open biomass burning smoke in aircraft and laboratory

715   studies, Atmos. Chem. Phys., 11, 12049-12064, https://doi.org/10.5194/acp-11-12049-2011, 2011.

716 Dai, Q., Schulze, B. C., Bi, X., Bui, A. A. T., Guo, F., Wallace, H. W., Sanchez, N. P., Flynn, J. H., Lefer,

717   B. L., Feng, Y., and Griffin, R. J.: Seasonal differences in formation processes of oxidized organic

718   aerosol near Houston, TX, Atmos. Chem. Phys., 19, 9641-9661, https://doi.org/10.5194/acp-19-9641-

719   2019, 2019.

720 Ding, A., Huang, X., Nie, W., Chi, X., Xu, Z., Zheng, L., Xu, Z., Xie, Y., Qi, X., Shen, Y., Sun, P., Wang,

721   J., Wang, L., Sun, J., Yang, X., Qin, W., Zhang, X., Cheng, W., Liu, W., Pan, L., and Fu, C.:

722   Significant reduction of PM2.5 in eastern China due to regional-scale emission control: evidence from

723   SORPES in 2011-2018, Atmos. Chem. Phys., 19, 11791-11801, https://doi.org/10.5194/acp-19-

724   11791-2019, 2019.

725 Docherty, K. S., Corse, E. W., Jaoui, M., Offenberg, J. H., Kleindienst, T. E., Krug, J. D., Riedel, T. P.,

726 and Lewandowski, M.: Trends in the oxidation and relative volatility of chamber-generated secondary

727 organic aerosol, Aerosol Sci. Tech., 52, 992-1004, https://doi.org/10.1080/02786826.2018.1500014,

728 2018.

729 Docherty, K. S., Stone, E. A., Ulbrich, I. M., DeCarlo, P. F., Snyder, D. C., Schauer, J. J., Peltier, R. E.,

730 Weber, R. J., Murphy, S. M., Seinfeld, J. H., Grover, B. D., Eatough, D. J., and Jimenez, J. L.:

731 Apportionment of Primary and Secondary Organic Aerosols in Southern California during the 2005

732 Study of Organic Aerosols in Riverside (SOAR-1), Environ. Sci. Technol., 42, 7655-7662,

733 https://doi.org/10.1021/es8008166, 2008.

734 Donahue, N. M., Robinson, A. L., Stanier, C. O., and Pandis, S. N.: Coupled Partitioning, Dilution, and

735 Chemical Aging of Semivolatile Organics, Environ. Sci. Technol., 40, 2635-2643,

736 https://doi.org/10.1021/es052297c, 2006.

737 Draxler, R. R., and Hess, G. D.: An overview of the HYSPLIT_4 modeling system for trajectories,

738 dispersion, and deposition, Aust. Meteor. Mag., 47, 295-308, 1998.

739 Duan, J., Huang, R., Gu, Y., Lin, C., Zhong, H., Wang, Y., Yuan, W., Ni, H., Yang, L., Chen, Y.,

740 Worsnop, D. R., and O'Dowd, C.: The formation and evolution of secondary organic aerosol during

741 summer in Xi'an: Aqueous phase processing in fog-rain days, Sci. Total Environ., 756, 144077,

742 https://doi.org/10.1016/j.scitotenv.2020.144077, 2021.

743 Fröhlich, R., Cubison, M. J., Slowik, J. G., Bukowiecki, N., Prévôt, A. S. H., Baltensperger, U.,

744 Schneider, J., Kimmel, J. R., Gonin, M., Rohner, U., Worsnop, D. R., and Jayne, J. T.: The ToF-

745 ACSM: a portable aerosol chemical speciation monitor with TOFMS detection, Atmos. Meas. Tech.,

746 6, 3225-3241, https://doi.org/10.5194/amt-6-3225-2013, 2013.

747 Fu, X., Wang, S., Xing, J., Zhang, X., Wang, T., and Hao, J.: Increasing Ammonia Concentrations

748 Reduce the Effectiveness of Particle Pollution Control Achieved via SO_2 and NOx Emissions

749 Reduction in East China, Environ. Sci. Technol. Lett., 4, 221-227,

750 https://doi.org/10.1021/acs.estlett.7b00143, 2017.

751 Fu, X., Wang, T., Gao, J., Wang, P., Liu, Y., Wang, S., Zhao, B., and Xue, L.: Persistent Heavy Winter

752 Nitrate Pollution Driven by Increased Photochemical Oxidants in Northern China, Environ. Sci.

753 Technol., 54, 3881-3889, https://doi.org/10.1021/acs.est.9b07248, 2020.

754 Ge, D., Nie, W., Sun, P., Liu, Y., Wang, T., Wang, J., Wang, J., Wang, L., Zhu, C., Wang, R., Liu, T.,

755 Chi, X., and Ding, A.: Characterization of particulate organic nitrates in the Yangtze River Delta, East

China, using the time-of-flight aerosol chemical speciation monitor, Atmos. Environ., 272, 118927, https://doi.org/10.1016/j.atmosenv.2021.118927, 2022.

Ge, X., Li, L., Chen, Y., Chen, H., Wu, D., Wang, J., Xie, X., Ge, S., Ye, Z., Xu, J., and Chen, M.: Aerosol characteristics and sources in Yangzhou, China resolved by offline aerosol mass spectrometry and other techniques, Environ. Pollut., 225, 74-85, https://doi.org/10.1016/j.envpol.2017.03.044, 2017.

Gilardoni, S., Massoli, P., Paglione, M., Giulianelli, L., Carbone, C., Rinaldi, M., Decesari, S., Sandrini, S., Costabile, F., Gobbi, G. P., Pietrogrande, M. C., Visentin, M., Scotto, F., Fuzzi, S., and Facchini, M. C.: Direct observation of aqueous secondary organic aerosol from biomass-burning emissions, P. Natl. Acad. Sci. USA, 113, 10013-10018, https://doi.org/10.1073/pnas.1602212113, 2016.

Guo, J., Zhou, S., Cai, M., Zhao, J., Song, W., Zhao, W., Hu, W., Sun, Y., He, Y., Yang, C., Xu, X., Zhang, Z., Cheng, P., Fan, Q., Hang, J., Fan, S., Wang, X., and Wang, X.: Characterization of submicron particles by time-of-flight aerosol chemical speciation monitor (ToF-ACSM) during wintertime: aerosol composition, sources, and chemical processes in Guangzhou, China, Atmos. Chem. Phys., 20, 7595-7615, https://doi.org/10.5194/acp-20-7595-2020, 2020.

Guo, L., Guo, X., Fang, C., and Zhu, S.: Observation analysis on characteristics of formation, evolution and transition of a long-lasting severe fog and haze episode in North China, Sci. China Earth Sci., 58, 329-344, https://doi.org/10.1007/s11430-014-4924-2, 2015.

Guo, S., Hu, M., Zamora, M. L., Peng, J., Shang, D., Zheng, J., Du, Z., Wu, Z., Shao, M., Zeng, L., Molina, M. J., and Zhang, R.: Elucidating severe urban haze formation in China, P. Natl. Acad. Sci. USA, 111, 17373-17378, https://doi.org/10.1073/pnas.1419604111, 2014.

He, K., Zhao, Q., Ma, Y., Duan, F., Yang, F., Shi, Z., and Chen, G.: Spatial and seasonal variability of PM2.5 acidity at two Chinese megacities: insights into the formation of secondary inorganic aerosols, Atmos. Chem. Phys., 12, 1377-1395, https://doi.org/10.5194/acp-12-1377-2012, 2012.

Heald, C. L., Kroll, J. H., Jimenez, J. L., Docherty, K. S., DeCarlo, P. F., Aiken, A. C., Chen, Q., Martin, S. T., Farmer, D. K., and Artaxo, P.: A simplified description of the evolution of organic aerosol composition in the atmosphere, Geophys. Res. Lett., 37, https://doi.org/10.1029/2010GL042737, 2010.

Herndon, S. C., Onasch, T. B., Wood, E. C., Kroll, J. H., Canagaratna, M. R., Jayne, J. T., Zavala, M. A., Knighton, W. B., Mazzoleni, C., Dubey, M. K., Ulbrich, I. M., Jimenez, J. L., Seila, R., de Gouw,

786   J. A., de Foy, B., Fast, J., Molina, L. T., Kolb, C. E., and Worsnop, D. R.: Correlation of secondary

787   organic aerosol with odd oxygen in Mexico City, Geophys. Res. Lett., 35,

788   https://doi.org/10.1029/2008GL034058, 2008.

789   Hinks, M. L., Montoya-Aguilera, J., Ellison, L., Lin, P., Laskin, A., Laskin, J., Shiraiwa, M., Dabdub,

790   D., and Nizkorodov, S. A.: Effect of relative humidity on the composition of secondary   organic

791   aerosol from the oxidation of toluene, Atmos. Chem. Phys., 18, 1643-1652,

792   https://doi.org/10.5194/acp-18-1643-2018, 2018.

793   Huang, R., Zhang, Y., Bozzetti, C., Ho, K., Cao, J., Han, Y., Daellenbach, K. R., Slowik, J. G., Platt, S.

794   M., Canonaco, F., Zotter, P., Wolf, R., Pieber, S. M., Bruns, E. A., Crippa, M., Ciarelli, G.,

795   Piazzalunga, A., Schwikowski, M., Abbaszade, G., Schnelle-Kreis, J., Zimmermann, R., An, Z.,

796   Szidat, S., Baltensperger, U., Haddad, I. E., and Prévôt, A. S. H.: High secondary aerosol contribution

797   to particulate pollution during haze events in China, Nature, 514, 218-222,

798   https://doi.org/10.1038/nature13774, 2014.

799   Huang, X., Zhang, J., Zhang, W., Tang, G., and Wang, Y.: Atmospheric ammonia and its effect on PM2.5

800   pollution in urban Chengdu, Sichuan Basin, China, Environ. Pollut., 291, 118195,

801   https://doi.org/10.1016/j.envpol.2021.118195, 2021.

802   Ianniello, A., Spataro, F., Esposito, G., Allegrini, I., Hu, M., and Zhu, T.: Chemical characteristics of

803   inorganic ammonium salts in PM2.5 in the atmosphere of Beijing (China), Atmos. Chem. Phys., 11,

804   10803-10822, https://doi.org/10.5194/acp-11-10803-2011, 2011.

805   Izhar, S., Gupta, T., and Panday, A. K.: Scavenging efficiency of water soluble inorganic and organic

806   aerosols by fog droplets in the Indo Gangetic Plain, Atmos. Res., 235, 104767,

807   https://doi.org/10.1016/j.atmosres.2019.104767, 2020.

808   Kim, H., Collier, S., Ge, X., Xu, J., Sun, Y., Jiang, W., Wang, Y., Herckes, P., and Zhang, Q.: Chemical

809   processing of water-soluble species and formation of secondary organic aerosol in fogs, Atmos.

810   Environ., 200, 158-166, https://doi.org/10.1016/j.atmosenv.2018.11.062, 2019.

811   Kong, L., Tan, Q., Feng, M., Qu, Y., An, J., Liu, X., Cheng, N., Deng, Y., Zhai, R., and Wang, Z.:

812   Investigating the characteristics and source analyses of PM2.5 seasonal variations in Chengdu,

813   Southwest China, Chemosphere, 243, 125267, https://doi.org/10.1016/j.chemosphere.2019.125267,

814   2020.

815   Kuang, Y., He, Y., Xu, W., Yuan, B., Zhang, G., Ma, Z., Wu, C., Wang, C., Wang, S., Zhang, S., Tao,

816   J., Ma, N., Su, H., Cheng, Y., Shao, M., and Sun, Y.: Photochemical Aqueous-Phase Reactions Induce

817   Rapid Daytime Formation of Oxygenated Organic Aerosol on the North China Plain, Environ. Sci.

818   Technol., 54, 3849-3860, https://doi.org/10.1021/acs.est.9b06836, 2020.

819 Lanz, V. A., Alfarra, M. R., Baltensperger, U., Buchmann, B., Hueglin, C., and Prévôt, A. S. H.: Source

820   apportionment of submicron organic aerosols at an urban site by factor analytical modelling of aerosol

821   mass spectra, Atmos. Chem. Phys., 7, 1503-1522, https://doi.org/10.5194/acp-7-1503-2007, 2007.

822 Li, H., Zhang, Q., Zheng, B., Chen, C., Wu, N., Guo, H., Zhang, Y., Zheng, Y., Li, X., and He, K.:

823   Nitrate-driven urban haze pollution during summertime over the North China Plain, Atmos. Chem.

824   Phys., 18, 5293-5306, https://doi.org/10.5194/acp-18-5293-2018, 2018.

825 Liu, M., Huang, X., Song, Y., Tang, J., Cao, J., Zhang, X., Zhang, Q., Wang, S., Xu, T., Kang, L., Cai,

826   X., Zhang, H., Yang, F., Wang, H., Yu, J. Z., Lau, A. K. H., He, L., Huang, X., Duan, L., Ding, A.,

827   Xue, L., Gao, J., Liu, B., and Zhu, T.: Ammonia emission control in China would mitigate haze

828   pollution and nitrogen deposition, but worsen acid rain, Proceedings of the National Academy of

829   Sciences, 116, 7760-7765, https://doi.org/10.1073/pnas.1814880116, 2019.

830 Liu, M., Huang, X., Song, Y., Xu, T., Wang, S., Wu, Z., Hu, M., Zhang, L., Zhang, Q., Pan, Y., Liu, X.,

831   and Zhu, T.: Rapid SO_2 emission reductions significantly increase tropospheric ammonia

832   concentrations over the North China Plain, Atmos. Chem. Phys., 18, 17933-17943,

833   https://doi.org/10.5194/acp-18-17933-2018, 2018.

834 Liu, P. S. K., Deng, R., Smith, K. A., Williams, L. R., Jayne, J. T., Canagaratna, M. R., Moore, K.,

835   Onasch, T. B., Worsnop, D. R., and Deshler, T.: Transmission Efficiency of an Aerodynamic

836   Focusing Lens System: Comparison of Model Calculations and Laboratory Measurements for the

837   Aerodyne Aerosol Mass Spectrometer, Aerosol Sci. Tech., 41, 721-733,

838   https://doi.org/10.1080/02786820701422278, 2007.

839 Liu, P., Ye, C., Xue, C., Zhang, C., Mu, Y., and Sun, X.: Formation mechanisms of atmospheric nitrate

840   and sulfate during the winter haze pollution periods in Beijing: gas-phase, heterogeneous and

841   aqueous-phase chemistry, Atmos. Chem. Phys., 20, 4153-4165, https://doi.org/10.5194/acp-20-4153-

842   2020, 2020.

843 Liu, T., Huang, D. D., Li, Z., Liu, Q., Chan, M., and Chan, C. K.: Comparison of secondary organic

844   aerosol formation from toluene on initially wet and dry ammonium sulfate particles at moderate

845   relative humidity, Atmos. Chem. Phys., 18, 5677-5689, https://doi.org/10.5194/acp-18-5677-2018,

846   2018.

847   Mandariya, A. K., Gupta, T., and Tripathi, S. N.: Effect of aqueous-phase processing on the formation

848   and evolution of organic aerosol (OA) under different stages of fog life cycles, Atmos. Environ., 206,

849   60-71, https://doi.org/10.1016/j.atmosenv.2019.02.047, 2019.

850   Matthew, B. M., Middlebrook, A. M., and Onasch, T. B.: Collection Efficiencies in an Aerodyne Aerosol

851   Mass Spectrometer as a Function of Particle Phase for Laboratory Generated Aerosols, Aerosol Sci.

852   Tech., 42, 884-898, https://doi.org/10.1080/02786820802356797, 2008.

853   Middlebrook, A. M., Bahreini, R., Jimenez, J. L., and Canagaratna, M. R.: Evaluation of Composition-

854   Dependent Collection Efficiencies for the Aerodyne Aerosol Mass Spectrometer using Field Data,

855   Aerosol Sci. Tech., 46, 258-271, https://doi.org/10.1080/02786826.2011.620041, 2012.

856   Mohr, C., DeCarlo, P. F., Heringa, M. F., Chirico, R., Slowik, J. G., Richter, R., Reche, C., Alastuey, A.,

857   Querol, X., Seco, R., Peñuelas, J., Jiménez, J. L., Crippa, M., Zimmermann, R., Baltensperger, U.,

858   and Prévôt, A. S. H.: Identification and quantification of organic aerosol from cooking   and other

859   sources in Barcelona using aerosol mass spectrometer data, Atmos. Chem. Phys., 12, 1649-1665,

860   https://doi.org/10.5194/acp-12-1649-2012, 2012.

861   Ng, N. L., Canagaratna, M. R., Jimenez, J. L., Chhabra, P. S., Seinfeld, J. H., and Worsnop, D. R.:

862   Changes in organic aerosol composition with aging inferred from aerosol mass spectra, Atmos. Chem.

863   Phys., 11, 6465-6474, https://doi.org/10.5194/acp-11-6465-2011, 2011.

864   Ng, N. L., Canagaratna, M. R., Zhang, Q., Jimenez, J. L., Tian, J., Ulbrich, I. M., Kroll, J. H., Docherty,

865   K. S., Chhabra, P. S., Bahreini, R., Murphy, S. M., Seinfeld, J. H., Hildebrandt, L., Donahue, N. M.,

866   DeCarlo, P. F., Lanz, V. A., Prévôt, A. S. H., Dinar, E., Rudich, Y., and Worsnop, D. R.: Organic

867   aerosol components observed in Northern Hemispheric datasets from Aerosol Mass Spectrometry,

868   Atmos. Chem. Phys., 10, 4625-4641, https://doi.org/10.5194/acp-10-4625-2010, 2010.

869   Ng, N. L., Herndon, S. C., Trimborn, A., Canagaratna, M. R., Croteau, P. L., Onasch, T. B., Sueper, D.,

870   Worsnop, D. R., Zhang, Q., Sun, Y. L., and Jayne, J. T.: An Aerosol Chemical Speciation Monitor

871   (ACSM) for Routine Monitoring of the Composition and Mass Concentrations of Ambient Aerosol,

872   Aerosol Sci. Tech., 45, 780-794, https://doi.org/10.1080/02786826.2011.560211, 2011.

873   Paatero, P., and Tapper, U.: Positive matrix factorization: A non-negative factor model with optimal

874   utilization of error estimates of data values, Environmetrics, 5, 111-126,

875   https://doi.org/10.1002/env.3170050203, 1994.

876   Paglione, M., Gilardoni, S., Rinaldi, M., Decesari, S., Zanca, N., Sandrini, S., Giulianelli, L., Bacco, D.,

877   Ferrari, S., Poluzzi, V., Scotto, F., Trentini, A., Poulain, L., Herrmann, H., Wiedensohler, A.,

878   Canonaco, F., Prévôt, A. S. H., Massoli, P., Carbone, C., Facchini, M. C., and Fuzzi, S.: The impact

879   of biomass burning and aqueous-phase processing on air quality: a multi-year source apportionment

880   study in the Po Valley, Italy, Atmos. Chem. Phys., 20, 1233-1254, https://doi.org/10.5194/acp-20-

881   1233-2020, 2020.

882   Pathak, R. K., Wu, W. S., and Wang, T.: Summertime PM2.5 ionic species in four major cities of China:

883   nitrate formation in an ammonia-deficient atmosphere, Atmos. Chem. Phys., 9, 1711-1722,

884   https://doi.org/10.5194/acp-9-1711-2009, 2009.

885   Peng, J., Hu, M., Shang, D., Wu, Z., Du, Z., Tan, T., Wang, Y., Zhang, F., and Zhang, R.: Explosive

886   Secondary Aerosol Formation during Severe Haze in the North China Plain, Environ. Sci. Technol.,

887   55, 2189-2207, https://doi.org/10.1021/acs.est.0c07204, 2021.

888   Polissar, A. V., Hopke, P. K., and Harris, J. M.: Source Regions for Atmospheric Aerosol Measured at

889   Barrow, Alaska, Environ. Sci. Technol., 35, 4214-4226, https://doi.org/10.1021/es0107529, 2001.

890   Rollins, A. W., Browne, E. C., Min, K., Pusede, S. E., Wooldridge, P. J., Gentner, D. R., Goldstein, A.

891   H., Liu, S., Day, D. A., and Russell, L. M.: Evidence for NOx control over nighttime SOA formation,

892   Science, 337, 1210-1212, 2012.

893   Song, M., Liu, X., Tan, Q., Feng, M., Qu, Y., An, J., and Zhang, Y.: Characteristics and formation

894   mechanism of persistent extreme haze pollution events in Chengdu, southwestern China, Environ.

895   Pollut., 251, 1-12, https://doi.org/10.1016/j.envpol.2019.04.081, 2019.

896   Sun, Y. L., Zhang, Q., Anastasio, C., and Sun, J.: Insights into secondary organic aerosol formed via

897   aqueous-phase reactions of phenolic compounds based on high resolution mass spectrometry, Atmos.

898   Chem. Phys., 10, 4809-4822, https://doi.org/10.5194/acp-10-4809-2010, 2010.

899   Sun, Y. L., Zhang, Q., Schwab, J. J., Demerjian, K. L., Chen, W. N., Bae, M. S., Hung, H. M., Hogrefe,

900   O., Frank, B., Rattigan, O. V., and Lin, Y. C.: Characterization of the sources and processes of organic

901   and inorganic aerosols in New York city with a high-resolution time-of-flight aerosol mass

902   apectrometer, Atmos. Chem. Phys., 11, 1581-1602, https://doi.org/10.5194/acp-11-1581-2011, 2011.

903   Sun, Y., Chen, C., Zhang, Y., Xu, W., Zhou, L., Cheng, X., Zheng, H., Ji, D., Li, J., Tang, X., Fu, P., and

904   Wang, Z.: Rapid formation and evolution of an extreme haze episode in Northern China during winter

905   2015, Sci. Rep.-UK, 6, https://doi.org/10.1038/srep27151, 2016.

906   Sun, Y., He, Y., Kuang, Y., Xu, W., Song, S., Ma, N., Tao, J., Cheng, P., Wu, C., Su, H., Cheng, Y., Xie,

907   C., Chen, C., Lei, L., Qiu, Y., Fu, P., Croteau, P., and Worsnop, D. R.: Chemical Differences Between

908   PM1 and PM2.5 in Highly Polluted Environment and Implications in Air Pollution Studies, Geophys.

909   Res. Lett., 47, https://doi.org/10.1029/2019GL086288, 2020.

910   Sun, Y., Jiang, Q., Xu, Y., Ma, Y., Zhang, Y., Liu, X., Li, W., Wang, F., Li, J., Wang, P., and Li, Z.:

911   Aerosol characterization over the North China Plain: Haze life cycle and biomass burning impacts in

912   summer, J. Geophys. Res.-Atmos., 121, 2508-2521, https://doi.org/10.1002/2015JD024261, 2016.

913   Tan, Z., Lu, K., Jiang, M., Su, R., Wang, H., Lou, S., Fu, Q., Zhai, C., Tan, Q., Yue, D., Chen, D., Wang,

914   Z., Xie, S., Zeng, L., and Zhang, Y.: Daytime atmospheric oxidation capacity in four Chinese

915   megacities during the photochemically polluted season: a case study based on box model simulation,

916   Atmos. Chem. Phys., 19, 3493-3513, https://doi.org/10.5194/acp-19-3493-2019, 2019.

917   Tao, J., Zhang, L., Cao, J., and Zhang, R.: A review of current knowledge concerning PM2. 5 chemical

918   composition, aerosol optical properties and their relationships across China, Atmos. Chem. Phys., 17,

919   9485-9518, https://doi.org/10.5194/acp-17-9485-2017, 2017.

920   Tian, M., Liu, Y., Yang, F., Zhang, L., Peng, C., Chen, Y., Shi, G., Wang, H., Luo, B., Jiang, C., Li, B.,

921   Takeda, N., and Koizumi, K.: Increasing importance of nitrate formation for heavy aerosol pollution

922   in two megacities in Sichuan Basin, southwest China, Environ. Pollut., 250, 898-905,

923   https://doi.org/10.1016/j.envpol.2019.04.098, 2019.

924   Ulbrich, I. M., Canagaratna, M. R., Zhang, Q., Worsnop, D. R., and Jimenez, J. L.: Interpretation of

925   organic components from Positive Matrix Factorization of aerosol mass spectrometric data, Atmos.

926   Chem. Phys., 9, 2891-2918, https://doi.org/10.5194/acp-9-2891-2009, 2009.

927   Wang, G., Zhang, R., Gomez, M. E., Yang, L., Levy Zamora, M., Hu, M., Lin, Y., Peng, J., Guo, S.,

928   Meng, J., Li, J., Cheng, C., Hu, T., Ren, Y., Wang, Y., Gao, J., Cao, J., An, Z., Zhou, W., Li, G.,

929   Wang, J., Tian, P., Marrero-Ortiz, W., Secrest, J., Du, Z., Zheng, J., Shang, D., Zeng, L., Shao, M.,

930   Wang, W., Huang, Y., Wang, Y., Zhu, Y., Li, Y., Hu, J., Pan, B., Cai, L., Cheng, Y., Ji, Y., Zhang,

931   F., Rosenfeld, D., Liss, P. S., Duce, R. A., Kolb, C. E., and Molina, M. J.: Persistent sulfate formation

932   from London Fog to Chinese haze, P. Natl. Acad. Sci. USA, 113, 13630-13635,

933   https://doi.org/10.1073/pnas.1616540113, 2016.

934   Wang, H., Tian, M., Chen, Y., Shi, G., Liu, Y., Yang, F., Zhang, L., Deng, L., Yu, J., Peng, C., and Cao,

935   X.: Seasonal characteristics, formation mechanisms and source origins of PM2.5 in two megacities in

936   Sichuan Basin, China, Atmos. Chem. Phys., 18, 865-881, https://doi.org/10.5194/acp-18-865-2018,

937   2018.

938   Wang, J., Ge, X., Chen, Y., Shen, Y., Zhang, Q., Sun, Y., Xu, J., Ge, S., Yu, H., and Chen, M.: Highly

939   time-resolved urban aerosol characteristics during springtime inYangtze River Delta, China: insights

940   from soot particle aerosol massspectrometry, Atmos. Chem. Phys., 16, 9109-9127,

941   https://doi.org/10.5194/acp-16-9109-2016, 2016.

942   Wang, J., Li, J., Ye, J., Zhao, J., Wu, Y., Hu, J., Liu, D., Nie, D., Shen, F., Huang, X., Huang, D. D., Ji,

943   D., Sun, X., Xu, W., Guo, J., Song, S., Qin, Y., Liu, P., Turner, J. R., Lee, H. C., Hwang, S., Liao, H.,

944   Martin, S. T., Zhang, Q., Chen, M., Sun, Y., Ge, X., and Jacob, D. J.: Fast sulfate formation from

945   oxidation of SO_2 by NO_2 and HONO observed in Beijing haze, Nat. Commun., 11,

946   https://doi.org/10.1038/s41467-020-16683-x, 2020.

947   Wang, J., Ye, J., Zhang, Q., Zhao, J., Wu, Y., Li, J., Liu, D., Li, W., Zhang, Y., Wu, C., Xie, C., Qin, Y.,

948   Lei, Y., Huang, X., Guo, J., Liu, P., Fu, P., Li, Y., Lee, H. C., Choi, H., Zhang, J., Liao, H., Chen, M.,

949   Sun, Y., Ge, X., Martin, S. T., and Jacob, D. J.: Aqueous production of secondary organic aerosol

950   from fossil-fuel emissions in winter Beijing haze, P. Natl. Acad. Sci. USA, 118,

951   https://doi.org/10.1073/pnas.2022179118, 2021.

952   Wang, Y., Yao, L., Wang, L., Liu, Z., Ji, D., Tang, G., Zhang, J., Sun, Y., Hu, B., and Xin, J.: Mechanism

953   for the formation of the January 2013 heavy haze pollution episode over central and eastern China,

954   Sci. China Earth Sci., 57, 14-25, https://doi.org/10.1007/s11430-013-4773-4, 2014.

955   Weimer, S., Alfarra, M. R., Schreiber, D., Mohr, M., Prévôt, A. S. H., and Baltensperger, U.: Organic

956   aerosol mass spectral signatures from wood-burning emissions: Influence of burning conditions and

957   wood type, J. Geophys. Res., 113, https://doi.org/10.1029/2007JD009309, 2008.

958   Wen, L., Xue, L., Wang, X., Xu, C., Chen, T., Yang, L., Wang, T., Zhang, Q., and Wang, W.:

959   Summertime fine particulate nitrate pollution in the North China Plain: increasing trends, formation

960   mechanisms and implications for control policy, Atmos. Chem. Phys., 18, 11261-11275,

961   https://doi.org/10.5194/acp-18-11261-2018, 2018.

962   Wu, L., Zhang, X., Sun, J., Wang, Y., Zhong, J., and Meng, Z.: Intensified wintertime secondary

963   inorganic aerosol formation during heavy haze pollution episodes (HPEs) in Beijing, China, J.

964   Environ. Sci.-China, https://doi.org/10.1016/j.jes.2022.01.008, 2022.

965   Xu, W., Croteau, P., Williams, L., Canagaratna, M., Onasch, T., Cross, E., Zhang, X., Robinson, W.,

Worsnop, D., and Jayne, J.: Laboratory characterization of an aerosol chemical speciation monitor with PM2.5 measurement capability, Aerosol Sci. Tech., 51, 69-83, https://doi.org/10.1080/02786826.2016.1241859, 2017.

Xu, W., Han, T., Du, W., Wang, Q., Chen, C., Zhao, J., Zhang, Y., Li, J., Fu, P., Wang, Z., Worsnop, D. R., and Sun, Y.: Effects of Aqueous-Phase and Photochemical Processing on Secondary Organic Aerosol Formation and Evolution in Beijing, China, Environ. Sci. Technol., 51, 762-770, https://doi.org/10.1021/acs.est.6b04498, 2017.

Yan, F., Chen, W., Jia, S., Zhong, B., Yang, L., Mao, J., Chang, M., Shao, M., Yuan, B., Situ, S., Wang, X., Chen, D., and Wang, X.: Stabilization for the secondary species contribution to PM2.5 in the Pearl River Delta (PRD) over the past decade, China: A meta-analysis, Atmos. Environ., 242, 117817, https://doi.org/10.1016/j.atmosenv.2020.117817, 2020.

Yu, L., Smith, J., Laskin, A., Anastasio, C., Laskin, J., and Zhang, Q.: Chemical characterization of SOA formed from aqueous-phase reactions of phenols with the triplet excited state of carbonyl and hydroxyl radical, Atmos. Chem. Phys., 14, 13801-13816, https://doi.org/10.5194/acp-14-13801-2014, 2014.

Zhai, S., Jacob, D. J., Wang, X., Liu, Z., Wen, T., Shah, V., Li, K., Moch, J. M., Bates, K. H., Song, S., Shen, L., Zhang, Y., Luo, G., Yu, F., Sun, Y., Wang, L., Qi, M., Tao, J., Gui, K., Xu, H., Zhang, Q., Zhao, T., Wang, Y., Lee, H. C., Choi, H., and Liao, H.: Control of particulate nitrate air pollution in China, Nat. Geosci., 14, 389-395, https://doi.org/10.1038/s41561-021-00726-z, 2021.

Zhan, B., Zhong, H., Chen, H., Chen, Y., Li, X., Wang, L., Wang, X., Mu, Y., Huang, R., George, C., and Chen, J.: The roles of aqueous-phase chemistry and photochemical oxidation in oxygenated organic aerosols formation, Atmos. Environ., 266, 118738, https://doi.org/10.1016/j.atmosenv.2021.118738, 2021.

Zhang, L., Guo, X., Zhao, T., Gong, S., Xu, X., Li, Y., Luo, L., Gui, K., Wang, H., Zheng, Y., and Yin, X.: A modelling study of the terrain effects on haze pollution in the Sichuan Basin, Atmos. Environ., 196, 77-85, https://doi.org/10.1016/j.atmosenv.2018.10.007, 2019.

Zhang, Q., Jimenez, J. L., Canagaratna, M. R., Ulbrich, I. M., Ng, N. L., Worsnop, D. R., and Sun, Y.: Understanding atmospheric organic aerosols via factor analysis of aerosol mass spectrometry: a review, Anal. Bioanal. Chem., 401, 3045-3067, https://doi.org/10.1007/s00216-011-5355-y, 2011.

Zhang, Q., Worsnop, D. R., Canagaratna, M. R., and Jimenez, J. L.: Hydrocarbon-like and oxygenated

organic aerosols in Pittsburgh: insights into sources and processes of organic aerosols, Atmos. Chem. Phys., 5, 3289-3311, https://doi.org/10.5194/acp-5-3289-2005, 2005.

Zhang, Y. W., Zhang, X. Y., Zhang, Y. M., Shen, X. J., Sun, J. Y., Ma, Q. L., Yu, X. M., Zhu, J. L., Zhang, L., and Che, H. C.: Significant concentration changes of chemical components of PM1 in the Yangtze River Delta area of China and the implications for the formation mechanism of heavy haze–fog pollution, Sci. Total Environ., 538, 7-15, https://doi.org/10.1016/j.scitotenv.2015.06.104, 2015.

Zhao, D., Liu, G., Xin, J., Quan, J., Wang, Y., Wang, X., Dai, L., Gao, W., Tang, G., Hu, B., Ma, Y., Wu, X., Wang, L., Liu, Z., and Wu, F.: Haze pollution under a high atmospheric oxidization capacity in summer in Beijing: insights into formation mechanism of atmospheric physicochemical processes, Atmos. Chem. Phys., 20, 4575-4592, https://doi.org/10.5194/acp-20-4575-2020, 2020.

Zhao, J., Qiu, Y., Zhou, W., Xu, W., Wang, J., Zhang, Y., Li, L., Xie, C., Wang, Q., Du, W., Worsnop, D. R., Canagaratna, M. R., Zhou, L., Ge, X., Fu, P., Li, J., Wang, Z., Donahue, N. M., and Sun, Y.: Organic Aerosol Processing During Winter Severe Haze Episodes in Beijing, J. Geophys. Res.-Atmos., 124, 10248-10263, https://doi.org/10.1029/2019JD030832, 2019.

Zhao, R., Mungall, E. L., Lee, A. K. Y., Aljawhary, D., and Abbatt, J. P. D.: Aqueous-phase photooxidation of levoglucosan – a mechanistic study using aerosol time-of-flight chemical ionization mass spectrometry (Aerosol ToF-CIMS), Atmos. Chem. Phys., 14, 9695-9706, https://doi.org/10.5194/acp-14-9695-2014, 2014.

Zheng, G. J., Duan, F. K., Su, H., Ma, Y. L., Cheng, Y., Zheng, B., Zhang, Q., Huang, T., Kimoto, T., Chang, D., Pöschl, U., Cheng, Y. F., and He, K. B.: Exploring the severe winter haze in Beijing: the impact of synoptic weather, regional transport and heterogeneous reactions, Atmos. Chem. Phys., 15, 2969-2983, https://doi.org/10.5194/acp-15-2969-2015, 2015.

Zheng, G., Duan, F., Ma, Y., Zhang, Q., Huang, T., Kimoto, T., Cheng, Y., Su, H., and He, K.: Episode-Based Evolution Pattern Analysis of Haze Pollution: Method Development and Results from Beijing, China, Environ. Sci. Technol., 50, 4632-4641, https://doi.org/10.1021/acs.est.5b05593, 2016.

Zhou, W., Chen, C., Lei, L., Fu, P., and Sun, Y.: Temporal variations and spatial distributions of gaseous and particulate air pollutants and their health risks during 2015–2019 in China, Environ. Pollut., 272, 116031, https://doi.org/10.1016/j.envpol.2020.116031, 2021.